Zhang, Y.J.; Ye, F.; Stanev, E.V.; Grashorn, S.:
Seamless cross-scale modeling with SCHISM
In: Ocean Modelling (2016) Elsevier

DOI: 10.1016/j.ocemod.2016.05.002

Seamless cross-scale modelling with SCHISM

Yinglong J. Zhang[a1], Fei Ye[a], Emil V. Stanev[b], and Sebastian Grashorn[b]

a. Virginia Institute of Marine Science,
College of William & Mary,
Center for Coastal Resource Management,
1375 Greate Road,
Gloucester Point, VA 23062,
USA

b. Helmholtz-Zentrum Geesthacht,
Max-Planck-Straße 1,
21502 Geesthacht,
Germany

[1] Corresponding author; e-mail: yjzhang@vims.edu; phone: (804) 684-7466; fax: (804) 684-7179.

Abstract

We present a new 3D unstructured-grid model (SCHISM) which is an upgrade from an existing model (SELFE). The new advection scheme for the momentum equation includes an iterative smoother to reduce excess mass produced by higher-order kriging method, and a new viscosity formulation is shown to work robustly for generic unstructured grids and effectively filter out spurious modes without introducing excessive dissipation. A new higher-order implicit advection scheme for transport (TVD^2) is proposed to effectively handle a wide range of Courant numbers as commonly found in typical cross-scale applications. The addition of quadrangular elements into the model, together with a recently proposed, highly flexible vertical grid system (Zhang et al. 2015), leads to model polymorphism that unifies 1D/2DH/2DV/3D cells in a single model grid. Results from several test cases demonstrate the model's good performance in the eddying regime, which presents greater challenges for unstructured-grid models and represents the last missing link for our cross-scale model. The model can thus be used to simulate cross-scale processes in a seamless fashion (i.e. from deep ocean into shallow depths).

Key words: SCHISM; eddying regime; baroclinic instability; general circulation; Black Sea

1 Introduction

For the past two decades, great progress has been made in the application of unstructured-grid (UG) models to coastal ocean processes. The superior boundary fitting and local refinement/derefinement ability of UG models make them ideally suited for nearshore applications involving complex geometry and bathymetry. In particular, the authors have previously demonstrated the great utility of UG models based on implicit time stepping schemes as the latter effectively bypass the stringent CFL constraint and thus removes one of the most severe restrictions in UG models (Zhang and Baptista 2008, hereafter ZB08); other time stepping methods such as predictor-corrector method have also been proposed with somewhat stricter time step limit than ours (but more relaxed than the explicit mode-splitting models) (Danilov 2012). The implicit UG models are free of mode-splitting errors and of the associated filter to prevent modes aliasing.

Despite the great success of implicit UG models for barotropic problems (e.g., tides, storm surge and tsunami inundations etc; Zhang et al. 2011, Bertin et al. 2014), their success for baroclinic problems remains modest so far due to some unique challenges in such applications (e.g. pressure-gradient errors, diapycnal mixing etc), which warrants further research effort. In fact, the success of UG models in the eddying regime has been very limited so far compared to their structured-grid counterpart, and one of the reasons is that the larger velocity space compared to the elevation space in UG models results in stronger spurious inertial modes that must be carefully controlled (Le Roux 2005; Ringler et al. 2010; Danilov 2012). Note that the spurious modes appear in all models (structured or unstructured), and can be excited from a variety of perturbation sources (Cotter and Ham 2011; Le Roux 2012), but they are particularly severe in larger depths and along steep slopes.

We have been systematically improving the baroclinic capability of our UG model, and this paper serves as a summary of the progress we have made in this endeavor for the past 5 years. Our experience suggests that for an UG model to work well in the baroclinic regimes from shallow to large depths, it has to strike a careful balance between accuracy, efficiency and robustness. For instance, the eddying regime sets a high standard for numerical dissipation and stability (control of modes), whereas the order of numerical schemes is less important in the estuarine applications, as the strong forcing therein favors stable and often lower-order numerical schemes. For such applications, more emphasis should be placed on faithfully resolving geometric and bathymetric features that act as the 1^{st}-order forcing for the underlying processes. The rich diversity of the processes as found from shallow to large depths likely precludes a 'one-size-fits-all' approach, and different numerical options may prove to be useful in different regimes. This has been the guiding principle when we built our cross-scale model.

As far as the model (SELFE) we have been developing for the past 15 years is concerned, we have made steady progress in the baroclinic regime in the *shallows* (ZB08; Burla 2010). Although all implicit models have inherent numerical diffusion, SELFE seems to have struck a good balance between numerical dissipation (due to implicit time stepping), numerical dispersion (due to Finite Element Method), and stability demanded by such type of applications. However, the following areas need to be improved before it can become a bona fide cross-scale model. First, the stratification is often under-estimated. This is related to the transport scheme as well as the vertical grid system used

(which is a hybrid system with part terrain-following *S* coordinates and part *Z* coordinates). The situation improves significantly with the introduction of TVD scheme for transport, and recently a flexible LSC^2 vertical grid (Zhang et al. 2015). Second, the model has not been applied in the eddying regime, which represents the last missing link for a truly cross-scale model. One of the main focuses of this paper is on improving the model in the eddying regime.

We have been working on a derivative product of the original SELFE model (v3.1dc; http://www.stccmop.org/knowledge_transfer/software/selfe; last accessed Sept. 17, 2015), mostly due to license disputes. However, the renaming of the model is probably long overdue as many important differences have emerged between our branch of SELFE and the original SELFE for the past 3 years. The new model, SCHISM (Semi-implicit Cross-scale Hydroscience Integrated System Model; www.schism.wiki, last accessed Sept. 17, 2015) is being distributed with an open-source Apache v2 license, and has been operationally tested by Central Weather Bureau of Taiwan (http://www.cwb.gov.tw/V7e/forecast/nwp/marine_forecast.htm; last accessed Sept. 17, 2015), California Department of Water Resource (http://baydeltaoffice.water.ca.gov/modeling/deltamodeling/models/bay_delta_schism/; last accessed Sept. 17, 2015), and National Laboratory of Civil Engineering, Portugal (LNEC; http://ariel.lnec.pt/node/40; last accessed Sept. 17, 2015). Although the original focus of SCHISM is the same as SELFE, i.e., hydrodynamic applications, it has since evolved into a comprehensive modeling framework (Fig. 1), courtesy of other developers and user groups (http://ccrm.vims.edu/schism/team.html, last accessed Sept. 17, 2015). At the moment the SCHISM modelling system includes: a wind-wave model (Roland et al 2012), 3 sediment transport models (Community Sediment Transport Model (Pinto et al. 2012), SED2D (Dodet 2013), and TIMOR (Zanke 2003)), 2 biological/ecological models (EcoSIM (Rodrigues et al. 2009) and CoSiNE, (Chai et al. 2002)), 2 oil spill models (Azevedo et al. 2014), an age tracer model based on the work of Shen and Haas (2004), a generic tracer model, and a water quality model (CE-QUAL-ICM, Cerco and Cole 1993). All modelling components have been parallelized using domain decomposition MPI with generally good scalability.

For clarity, we list out the main new features of SCHISM as compared to SELFE v3.1dc:

1) Vertical grid system (LSC^2, Zhang et al. 2015);
2) Mixed triangular-quadrangular horizontal grid;
3) Implicit advection scheme for transport (TVD^2);
4) Advection scheme for momentum: optional higher-order kriging with ELAD filter;
5) A new horizontal viscosity scheme (including bi-harmonic viscosity) to effectively filter out inertial spurious modes without introducing excessive dissipation.

The 1st feature has been reported in Zhang et al. (2015), and the rest will be the subject of this paper.

To prepare for the introduction of the new SCHISM features, we will first briefly review some key formulations in SELFE in Section 2, with the focus on the treatment of momentum advection. We then present the main differences and new developments of SCHISM in Section 3, including the new advection schemes for momentum and transport equations, and a filter-like bi-harmonic viscosity. Section 4 shows the extension of the formulations to mixed triangular-quadrangular grids. Several challenging test cases are presented in Section 5 to benchmark the model in the eddying regime. Together with previously demonstrated model capability in the non-eddying regimes, the new capability in the eddying regime brings forth a seamless cross-scale model that is equally skillful from shallow to deep oceans. Section 6 concludes the paper.

2. SELFE formulation

To clearly show the new revisions in SCHISM, in this section we briefly review some key formulations in SELFE v3.1dc (ZB08). SELFE solves the Reynolds-averaged Navier-Stokes equation in its hydrostatic form and transport of salt and heat:

Momentum equation: $$\frac{D\mathbf{u}}{Dt} = \frac{\partial}{\partial z}\left(\nu \frac{\partial \mathbf{u}}{\partial z}\right) - g\nabla\eta + \mathbf{F}, \quad (1)$$

Continuity equation in 3D and 2D depth-integrated forms:

$$\nabla \cdot \mathbf{u} + \frac{\partial w}{\partial z} = 0\,, \tag{2}$$

$$\frac{\partial \eta}{\partial t} + \nabla \cdot \int_{-h}^{\eta} \mathbf{u} dz = 0, \tag{3}$$

Transport equations:

$$\frac{\partial C}{\partial t} + \nabla \cdot (\mathbf{u}C) = \frac{\partial}{\partial z}\left(\kappa \frac{\partial C}{\partial z}\right) + F_h, \tag{4}$$

where

	∇	$\left(\frac{\partial}{\partial x}, \frac{\partial}{\partial y}\right)$
	D/Dt	material derivative
	(x,y)	horizontal Cartesian coordinates
	z	vertical coordinate, positive upward
	t	time
	$\eta(x,y,t)$	free-surface elevation
	$h(x,y)$	bathymetric depth
	$\mathbf{u}(x,y,z,t)$	horizontal velocity, with Cartesian components (u,v)
	w	vertical velocity
	$\boldsymbol{F}$	other forcing terms in momentum (baroclinic gradient $(-\frac{g}{\rho_0}\int_z^{\eta}\nabla\rho d\zeta)$, horizontal viscosity, Coriolis, earth tidal potential, atmospheric pressure, radiation stress)
	g	acceleration of gravity, in [ms^{-2}]
	C	tracer concentration (e.g., salinity, temperature, sediment etc)
	ν	vertical eddy viscosity, in [m^2s^{-1}]
	κ	vertical eddy diffusivity, for tracers, in [m^2s^{-1}]
	F_h	horizontal diffusion and mass sources/sinks

The differential system (1-4) is closed with turbulence closure of the generic length-scale model of Umlauf and Burchard (2003), and proper initial and boundary conditions (B.C.) for each differential equation.

The 3D domain is first discretized into triangular elements in the horizontal and a series of vertical layers (using hybrid *SZ* coordinates). The unknown variables are then staggered on triangular prisms as shown in Fig. 2, which resembles a CD grid (Arakawa and Lamb 1977) as well as the P^1-P^{NC} element configuration (Le Roux et al. 2005).

In the first step, SELFE solves the coupled equations (1) and (3) together with their boundary conditions, with a semi-implicit Galerkin Finite Element method (FEM). The linear pair of P^1-P^{NC} element configuration is used to approximate the elevation and horizontal velocity respectively. The implicit terms include elevation gradient, vertical viscosity, the bottom B.C. for Eq. (1), and the divergence term in Eq. (3), all of which impose severe stability constraints. The time stepping is done using a 2nd-order Crank-Nicolson method, i.e., with the implicitness factor being 0.5 (in practice a value slightly larger than 0.5 is used for robustness). The unknown velocities (defined at side centers) are first eliminated from the equations with the aid from the bottom boundary layer, resulting in an integral equation for the unknown elevations alone, which can be efficiently solved with a parallel solver (Jacobian Conjugate Gradient)

(ZB08). The momentum equation is then solved with a Galerkin FEM along each vertical column of a side. After the horizontal velocity and elevation are found, the vertical velocity is then solved from Eq. (2) with a Finite Volume method (FVM) along each prism. The volume conservation ensured by FVM serves as the foundation for the mass conservative transport solver, which also employs a FVM (with either 1st-order upwind or 2nd-order explicit TVD method; see Casulli and Zanolli 2005), because the volume conservation guarantees constancy condition for the transport equation. Note that there is a closure error for the vertical velocity due to the different methods used to solve the two forms of the continuity equation (FEM vs FVM). Solution of the 2.5 turbulence closure equations and update of the vertical grid (including the marking of wetting and drying nodes/sides/elements) constitute the remaining operations in a time stepping loop. More details can be found in ZB08.

The CD grid used in SELFE is instrumental in its ability to easily maintain geostrophic balance, as both velocity components (u,v) are explicitly modelled. This is a key difference from UnTRIM-family of models (Casulli and Cattani 1994) which uses a C grid, where special treatment has to be made to properly maintain the geostrophic balance (Zhang et al. 2004; Ham et al. 2007). In addition, due to the finite-difference method used in the UnTRIM-family of models, only *orthogonal* UG grids can be used, which proves to be restrictive in practice. On the other hand, the FEM framework used in SELFE (and SCHISM) allows generic non-orthogonal UG's to be used. In fact, the model has a high tolerance for skew (non-orthogonal) elements.

A critical feature of SELFE is the use of Eulerian-Lagrangian method (ELM) to treat the momentum advection term:

$$\frac{D\mathbf{u}}{D\mathrm{t}} \cong \frac{\mathbf{u}(\mathbf{x}, t^{n+1}) - \mathbf{u}(\mathbf{x}^*, t^n)}{\Delta t} \tag{5}$$

where 'n' and 'n+1' denote time step levels, Δt is the time step, $\mathbf{x}$ is a shorthand for (x,y,z), and $\mathbf{x}^*$ is the location of the foot of characteristic line (FOCL), calculated from the characteristic equation:

$$\frac{D\mathbf{x}}{D\mathrm{t}} = \mathbf{u} \tag{6}$$

The location $\mathbf{x}^*$ is found via a backtracking step, standard in an ELM, via backward integration of Eq. (6) starting from a *given* location ($\mathbf{x}$), which is in our case a side center at whole level where the horizontal velocity $\mathbf{u}$ is defined. The fixed starting location (Eulerian framework) followed by a Lagrangian tracking step gives the name Eulerian-Lagrangian method. Therefore the ELM consists of two major steps: a backtracking step (Fig. 3a) and an interpolation step at FOCL (Fig. 3b). We further sub-divide the tracking step into smaller intervals (based on local flow gradients), and use a 2nd-order Runge-Kutta method (mid-point method) within each interval, in order to accurately track the trajectory (cf. the ELM test in Section 3). Although exact integration methods have been proposed (Ham et al. 2006), their implementation is complicated for a 3D (triangular and quadrangular) prism and in the exceptional cases of wetting and drying interfaces. The interpolation step serves as an important control for numerical diffusion/dispersion in the ELM, and we therefore experimented with several options as shown below. However, before we get to this, we first explain how SELFE converts the velocities at sides to the velocities at nodes, as the latter are required in the interpolation of the velocities along the characteristic line and at FOCL (Fig. 3ab).

As explained by Danilov (2012), the conversion method used bears important ramifications: judicious averaging (e.g., from side to elements or to node etc.) may greatly reduce the need later on for filters to remove the inertial spurious modes while still keeping the inherent numerical dissipation low. In fact, one could have used the discontinuous velocity calculated within each element to carry out the backtracking, but this would introduce insufficient amount of dissipation to suppress the inertial modes.

In the first approach ('MA' hereafter), we use inverse distance weights to interpolate from velocities at surrounding sides onto a node (Fig. 4a). This introduces diffusion which may be excessive in our experience, and therefore no further stabilization (via filters or viscosity) is required for this approach (see the discussion of stabilization in Danilov 2012). This approach works well in shallow waters especially for the inundation process, as numerical stability often trumps the order of accuracy there. The 2nd approach ('MB' hereafter) is more elegant and utilizes the (linear) shape function in FEM within each element to calculate the node velocities. This is equivalent to using the P^{NC} non-conformal shape function (Le Roux et al. 2005) as one essentially interpolates based on information at sides (Fig. 4b). Because each element produces a velocity vector at each of its 3 nodes, the final node velocity is the simple average of the values calculated from all of the surrounding elements (Fig. 4b). As we will demonstrate with a simple test in the next section, this approach introduces much less dissipation, but does exhibit inertial spurious modes. As a result,

196 further stabilization is required. To this end, SELFE uses a 5-point Shapiro filter (Shapiro 1970) as illustrated in Fig.
197 5a; the velocity at a side '0' is filtered as:

198 $$\tilde{\mathbf{u}}_0 = \mathbf{u}_0 + \frac{\gamma}{4}(\mathbf{u}_1 + \mathbf{u}_2 + \mathbf{u}_3 + \mathbf{u}_4 - 4\mathbf{u}_0), \quad (7)$$

199 with the strength usually set as γ=0.5. We will show that the filter is analogous to a viscosity implementation in the
200 next section. It proves to be very effective in removing the sub-grid scale inertial spurious modes; however, it
201 introduces too much dissipation in the eddying regime, and we'll present a better alternative in SCHISM in the next
202 section.

203 Once the node velocities are found via MA or MB, the interpolation at the FOCL is carried out in 3D space. A simple
204 linear interpolation is used in the vertical dimension as the results from the cubic-spline interpolation turned out to be
205 similar, due to more confined spatial scales and smaller grid sizes in the vertical. The horizontal interpolation can be
206 done using either a simple linear shape function based on all of the nodes of the containing element ('LI' hereafter;
207 Fig. 3b), or a higher-order dual kriging method ('KR' hereafter) suggested by Le Roux et al. (1997). The latter requires
208 larger stencil around the FOCL, and for best parallel efficiency we use a 2-tier neighborhood as shown in Fig. 3b.
209 Given a total of N nodes available in the 2-tier neighborhood, the interpolation function is constructed as (Le Roux
210 1997):

211 $$f^h(x,y) = (\alpha_1 + \alpha_2 x + \alpha_3 y) + \sum_{i=1}^{N} \beta_i K(r_i) \quad (8)$$

212 where the first 3 RHS terms inside the parentheses represent a mean drift (modeled as a linear function), and the 2nd
213 terms is the fluctuation part, α_j, β_i are unknown coefficients, and r_i is the distance between (x,y) and (x_i,y_i), with i being
214 a node. The following forms of the generalized covariance function are commonly used (Le Roux et al. 1997):

215 $$K(r) = -r,\ r^2\log(r),\ r^3,\ -r^5,\ r^7 \quad (9)$$

216 with increasing dispersion for the higher-degree functions; therefore in practice, the last two functions are seldom
217 used. In the following we will refer to the first 3 functions as 'KR1', 'KR2' and 'KR3' respectively.

218 The equations to solve for the unknown coefficients are:

219 $$\begin{cases} f^h(x_i,y_i) = d_i, \quad 1 \le i \le N \\ \sum_{i=1}^{N} \beta_i = 0 \\ \sum_{i=1}^{N} x_i \beta_i = 0 \\ \sum_{i=1}^{N} y_i \beta_i = 0 \end{cases} \quad (10)$$

220 where d_i are given data at each node. The 1st equation in (10) indicates that the dual kriging is an exact interpolator,
221 and the other 3 equations are derived from minimization of the variance of estimation error (Le Roux et al. 1997).
222 Note that the matrix of Eq. (10) is dependent only on geometry and therefore can be inverted and stored before the
223 time stepping loop to achieve greater efficiency. After the coefficients are found, the interpolation at FOCL is done
224 via Eq. (8).

225 The smaller stencil used here compared to that used by Le Roux et al. (1997) leads to larger numerical dispersion.
226 Therefore an effective method must be found to control the dispersion, and we will show how this is done in SCHISM
227 in the next section.

228 We conclude this section by noting that the various schemes presented above can be freely combined, resulting in
229 schemes like 'MA-LI', 'MB-KR2' etc.

230

3. Revisions in SCHISM

In this section we present new advection schemes for the transport and momentum equations used by SCHISM. Our focus is on the eddying regime but the reduced dissipation enabled by the new schemes proves largely beneficial for the shallow environment as well and we have successfully tested these schemes in the non-eddying regime (Ye et al. submitted).

3.1 Tracer advection scheme: TVD^2

The 2nd-order TVD scheme in SELFE is explicit in 3D space and thus subject to the Courant condition, which comprises of horizontal and vertical fluxes across each of the prism faces (Casulli and Zanolli 2005). The restriction related to the vertical fluxes is especially severe due to smaller grid size used in the vertical dimension, and therefore a large number of sub-cycles within each time step are usually required. To partially mitigate the issue, a hybrid upwind-TVD approach can be used in which the more efficient upwind scheme, with an implicit treatment of the vertical fluxes, is used when the flow depth falls below a given threshold (with the assumption that stratification is usually much smaller in the shallows). However, this approach does not work in deeper depths of eddying regime, as large vertical velocities are not uncommon along steep bathymetric slopes. Together with the fact that a large number of vertical levels are usually required in the eddying regime, the explicit scheme leads to subpar computational performance and usually takes over 90% of the total CPU time.

We therefore develop an implicit TVD scheme in the vertical dimension in SCHISM. We start from the FVM formulation of the 3D transport equation (4) at a prism i:

$$C_i^{n+1} = C_i^n - \frac{\Delta t}{V_i}\sum_{j\in S^-}|Q_j|(C_i - C_j) - \frac{\Delta t}{V_i}\sum_{j\in S} Q_j C_{jr} + \frac{A_i \Delta t}{V_i}\left[\left(\kappa\frac{\partial C}{\partial z}\right)_{i,k} - \left(\kappa\frac{\partial C}{\partial z}\right)_{i,k-1}\right] + \frac{\Delta t}{V_i}\int_{V_i} F_h dV \quad (11)$$

where C_j is the concentration at the neighboring prism of i across a prism face $j \in S = S^+ \cup S^-$, with S^+/S^- denoting outflow/inflow faces (which can be horizontal or vertical) respectively, V_i is the prism volume, A_i is the area of the associated surficial triangular element, and Q_j is the flux at a face. In Eq. (11) we have utilized the volume conservation in a prism (which is enforced by the solution of the vertical velocity): $\sum_{j\in S^-}|Q_j| = \sum_{j\in S^+}|Q_j|$. We have also approximated the concentration at a face as the sum of an upwind and a correction part as:

$$C\big|_j = C_{jup} + C_{jr}. \quad (12)$$

Note that in the 2nd term of RHS of Eq. (11), we have $C_j = C_{jup}$ as j is an inflow face. In addition, we have intentionally left out the time level in some terms in (11) as they will be treated explicitly or implicitly in the following.

We split the solution of Eq. (11) into 3 sub-steps:

$$C_i^{m+1} = C_i^n + \frac{\Delta t_m}{V_i}\sum_{j\in S_H^-}|Q_j|(C_j^m - C_i^m) - \frac{\Delta t_m}{V_i}\sum_{j\in S_H} Q_j \hat{\psi}_j^m, \quad (m = 1,...,M) \quad (13)$$

$$\tilde{C}_i = C_i^{M+1} + \frac{\Delta t}{V_i}\sum_{j\in S_V^-}|Q_j|(\tilde{C}_j - \tilde{C}_i) - \frac{\Delta t}{V_i}\sum_{j\in S_V} Q_j(\Phi_j + \Psi_j), (j = k_b,.., N_z) \quad (14)$$

$$C_i^{n+1} = \tilde{C}_i + \frac{A_i \Delta t}{V_i}\left[\left(\kappa\frac{\partial C}{\partial z}\right)_{i,k}^{n+1} - \left(\kappa\frac{\partial C}{\partial z}\right)_{i,k-1}^{n+1}\right] + \frac{\Delta t}{V_i}\int_{V_i} F_h^n dV, (k = k_b,.., N_z) \quad (15)$$

The 1st step Eq. (13) solves the horizontal advection part (for all 3D prisms i), the 2nd step Eq. (14) deals with the vertical advection part (where k_b is the bottom level index and N_z is the surface level index), and the last step Eq. (15) tackles the remaining terms. We could have combined the 1st and 3rd steps into a single step at the expense of efficiency, because sub-cycling is used in the 1st step. In Eq. (13), sub-cylcing in M sub-steps is required because of the horizontal Courant number condition, Δt_m is the sub-time step used, and $\hat{\psi}_j^m$ is a standard TVD limiter function. Eq. (13) is then

solved with a standard TVD method. The last step (15) requires the solution of a simple tri-diagonal matrix. So we will only focus on the 2nd step.

Following Duraisamy and Baeder (2007, hereafter DB07), we use two limiter functions in Eq. (14): Φ_j is the space limiter and Ψ_j is the time limiter – thus the name TVD^2. The origin of these two limiters is the approximation Eq. (12) via a Taylor expansion in both space *and* time (DB07):

$$C_j^{n+1/2} = C_{jup}^{n+1} + \Phi_j + \Psi_j = C_{jup}^{n+1} + \mathbf{r} \bullet [\nabla C]_{jup}^{n+1} - \frac{\Delta t}{2}[\frac{\partial C}{\partial t}]_{jup}^{n+1} \tag{16}$$

Note that the interface value is taken at time level n+1/2 to gain 2nd-order accuracy in time. The vector **r** points from prism center *jup* to face center *j*. Due to the operator splitting method, C^{n+1} now actually corresponds to $\tilde{\tilde{C}}$. Customary in a TVD method, we then replace the last 2 terms with limiter functions:

$$C_j^{n+1/2} = \tilde{\tilde{C}}_{jup} + \frac{\phi_j}{2}(\tilde{\tilde{C}}_{jD} - \tilde{\tilde{C}}_{jup}) - \frac{\psi_j}{2}(\tilde{\tilde{C}}_{jup} - C_{jup}^{M+1}) \tag{17}$$

and so:

$$\Phi_j = \frac{\phi_j}{2}(\tilde{\tilde{C}}_{jD} - \tilde{\tilde{C}}_{jup}), \Psi_j = -\frac{\psi_j}{2}(\tilde{\tilde{C}}_{jup} - C_{jup}^{M+1}) \tag{18}$$

where '*jD*' stands for the downwind prism of *i* along the face *j*, and ϕ_j and ψ_j are 2 limiter functions in space and time respectively. Note that $\phi_j = \psi_j = 1$ leads to 2nd-order accuracy in both space and time.

Substituting Eq. (18) into (14) and after some algebra we obtain a nonlinear equation for the unknown concentration:

$$\tilde{\tilde{C}}_i + \frac{\frac{\Delta t}{V_i}\sum_{j\in S_V^-}|Q_j|\left[1+\frac{1}{2}\left(\sum_{p\in S_V^+}\frac{\phi_p}{r_p} - \phi_j\right)\right](\tilde{\tilde{C}}_i - \tilde{\tilde{C}}_j)}{1+\frac{\Delta t}{2V_i}\sum_{j\in S_V^+}|Q_j|(\sum_{q\in S_V^-}\frac{\psi_q}{s_q} - \psi_j)} = C_i^{M+1} \tag{19}$$

where r_p and s_q are upwind and downwind ratios respectively:

$$r_p = \frac{\sum_{q\in S_V^-}|Q_q|(\tilde{\tilde{C}}_q - \tilde{\tilde{C}}_i)}{|Q_p|(\tilde{\tilde{C}}_i - \tilde{\tilde{C}}_p)}, p \in S_V^+$$
$$s_q = \frac{(\tilde{\tilde{C}}_i - C_i^{M+1})\sum_{p\in S_V^+}|Q_p|}{|Q_q|(\tilde{\tilde{C}}_q - C_q^{M+1})}, q \in S_V^- \tag{20}$$

DB07 showed that a sufficient TVD condition for Eq. (19) is that the coefficient of the 2nd LHS term be non-negative, i.e.:

$$1+\frac{1}{2}\left(\sum_{p\in S_V^+}\frac{\phi_p}{r_p} - \phi_j\right) \geq 0 \tag{21}$$

$$1+\frac{\Delta t}{2V_i}\sum_{j\in S_V^+}|Q_j|(\sum_{q\in S_V^-}\frac{\psi_q}{s_q} - \psi_j) \geq \delta > 0 \tag{22}$$

where δ is a small positive number. Eq. (21) can be satisfied with any choice of standard limiter functions in space, and Eq. (22) must be solved together with Eq. (19) iteratively, because ψ and s_q are functions of $\tilde{C}$. We need to discuss 3 scenarios for prism *i*:

(1) vertically convergent flow: in this case, the outer sum in Eq. (22) is 0, so the inequality is always true;

(2) divergent flow: the numerator of the 2nd LHS term in Eq. (19) is 0, and so $\tilde{C}_i = C_i^{M+1}$;

(3) uni-directional flow (either upward or downward): in this case, prism *i* has exactly 1 inflow and 1 outflow face vertically, so a sufficient condition for Eq. (22) is:

$$1 - \frac{\Delta t}{2V_i} |Q_j| \psi_j \geq \delta > 0, \; j \in S_V^+ \tag{23}$$

Therefore we choose the following form for the limiter:

$$\psi_j = \max\left[0, \min\left[1, \frac{2(1-\delta)V_i}{|Q_j|\Delta t}\right]\right], \; j \in S_V^+ \tag{24}$$

where we have imposed a maximum of 1 in an attempt to obtain 2nd-order accuracy in time. Note that the limiter is a function of the vertical Courant number: it decreases as the Courant number increases. Eqs. (19) and (24) are then solved using a simple Picard iteration method starting from ψ=0 everywhere, and fast convergence within a few iterations is usually observed.

Simple benchmark tests indicate that TVD^2 is accurate for a wide range of Courant numbers as found in typical geophysical flows (Ye et al. submitted). The accuracy and efficiency of TVD^2 will also be shown in Section 5. It works equally well in eddying and non-eddying regimes, from very shallow to very deep depths, and is thus ideal for cross-scale applications.

3.2 Viscosity

Danilov (2012) demonstrated the importance of the momentum advection and stabilization schemes in the eddying regime for UG models. Beside accuracy consideration, prevention of spurious modes is an important goal, which can be done via viscosity, filtering, and/or averaging of velocity fields (e.g., from element to node etc). As the Shapiro filter, which is designed to remove the spurious modes in SELFE, is too dissipative in the eddying regime, we replace it with an effective horizontal viscosity scheme in SCHISM.

Most geophysical fluid dynamic models use horizontal viscosity to add dissipation to the numerical scheme in order to control sub-grid scale instabilities, e.g. due to cascading of enstrophy toward the smallest resolved scales (Griffies and Hallberg 2000). In other words, one of the main goals of the viscosity is to remove the unresolved sub-grid scales but preserve the resolved scales as much as possible. The new viscosity scheme presented here is therefore designed more to filter out spurious modes than to represent the actual physical horizontal mixing process.

We start with a demonstration that the traditional Laplacian viscosity loses its effectiveness on generic UGs. While there are different ways to implement the Laplacian viscosity on UGs, we present a particular way catered to the specificity of SCHISM; nevertheless the conclusion here applies to other implementations as well. Consider the stencil depicted in Fig. 5a; the horizontal viscosity term at the side center '0' is given by:

$$\nabla \cdot (\mu \nabla u)\big|_0 \cong \frac{\mu_0}{A_I + A_{II}} \oint_\Gamma \frac{\partial u}{\partial n} d\Gamma \tag{25}$$

where Γ is the boundary PQRS (Fig. 5a), and we assume the viscosity μ_0 to be constant in the stencil. The formula for the viscosity term for the *v*-velocity is similar. The derivatives are evaluated using the linear shape functions defined inside the 2 smaller triangles formed by joining the 3 side centers (012 and 034 in Fig. 5a), and are constant within each triangle:

$$\left.\frac{\partial u}{\partial x}\right|_I = \frac{1}{A_I}\left[u_1(y_Q - y_P) + u_2(y_R - y_Q) + u_0(y_P - y_R)\right]$$
$$\left.\frac{\partial u}{\partial y}\right|_I = -\frac{1}{A_I}\left[u_1(x_Q - x_P) + u_2(x_R - x_Q) + u_0(x_P - x_R)\right] \quad (26)$$

with a similar form for element *II*. The final form for the viscosity is then:

$$\nabla\cdot(\mu\nabla u)\big|_0 = \frac{\mu_0}{A_I + A_{II}}\left\{\begin{array}{l}\frac{1}{A_I}\left[u_1\overrightarrow{PQ}\cdot\overrightarrow{PR} + u_2\overrightarrow{RQ}\cdot\overrightarrow{RP} - u_0|\overrightarrow{PR}|^2\right] + \\ \frac{1}{A_{II}}\left[u_3\overrightarrow{RP}\cdot\overrightarrow{RS} + u_4\overrightarrow{PR}\cdot\overrightarrow{PS} - u_0|\overrightarrow{PR}|^2\right]\end{array}\right\} \quad (27)$$

where proper linear vertical interpolation has been made to bring u_m (m=1,..,4) onto the same horizontal plane as u_0. For uniform grid with equilateral triangles, Eq. (27) becomes:

$$\nabla\cdot(\mu\nabla u)\big|_0 = \frac{\mu_0}{\sqrt{3}A_I}(u_1 + u_2 + u_3 + u_4 - 4u_0) \quad (28)$$

which is equivalent to the 5-point Shapiro filter (cf. Eq. (7)), with filter strength $\gamma = \frac{4\mu_0\Delta t}{\sqrt{3}A_I} \equiv \frac{4D}{\sqrt{3}}$ (with D being a diffusion number). However, for obtuse triangles, some coefficients of u_m (m=1,2,3,4) in Eq. (27) become negative, and the viscosity then behaves like an amplifier (Shapiro 1970), and thus loses its utility of smoothing. This calls for a filter-like viscosity implementation as in Eq. (28) for UGs, and we use this equation to replace the Shapiro filter for generic UG's. Danilov and Androsov (2015) used a similar form for viscosity. For boundary sides the viscosity term is omitted as B.C. is applied there instead.

The bi-harmonic viscosity is often superior to the Laplacian viscosity as it is more discriminating in removing sub-grid instabilities without adversely affecting the resolved scales of flow (Griffies and Hallberg 2000). The bi-harmonic viscosity can be implemented by applying the Laplacian operator twice. Referring to Fig. 5c, we have:

$$-\lambda\nabla^4 u\big|_0 = -\lambda\gamma_3(\nabla^2 u_1 + \nabla^2 u_2 + \nabla^2 u_3 + \nabla^2 u_3 - 4\nabla^2 u_0) =$$
$$\frac{\gamma_2}{\Delta t}\left[7(u_1 + u_2 + u_3 + u_4) - u_{1a} - u_{1b} - u_{2a} - u_{2b} - u_{3a} - u_{3b} - u_{4a} - u_{4b} - 20u_0\right] \quad (29)$$

where λ is a hyper viscosity in m^4/s, $\gamma_3 = 1/(\sqrt{3}A_I)$ and $\gamma_2 = \lambda\gamma_3^2\Delta t$ is a diffusion-number-like dimensionless constant. We found that in practice $\gamma_2 \le 0.025$ is sufficient to suppress inertial spurious modes, and so in this paper we set γ_2=0.025 for all test cases.

3.3 Momentum advection scheme

As we discussed in Section 2, the interpolation method used at FOCL has important ramifications. Since the dual kriging interpolators generate numerical dispersion (over-/under-shoots or excess mass field), we need an effective method to control the excess mass field; otherwise the dispersion would severely aggravate the inertial spurious modes. We use the ELAD method of Shchepetkin and McWilliams (1998) for this purpose. The essence of ELAD is to iteratively diffuse the *excess field*, instead of the original signal, using a diffusion operator/smoother. The viscosity scheme presented in the previous sub-section is used as the diffusion operator. The procedure is summarized as follows:

1) Find the local max/min at FOCL. Assuming that the prism at FOCL starting from a side *j* and level *k* is (*kf*,*nf*), where *nf* is the element index and *kf* is the vertical index, the max/min are found in the prism (*kf*,*nf*) as:

$$u_{k,j}^{\max} = \max_{l=1:3,k=-1,0} u_{kf+k,im(l,nf)}$$
$$u_{k,j}^{\min} = \min_{l=1:3,k=-1,0} u_{kf+k,im(l,nf)} \quad (30)$$

where *im*() enumerates 3 nodes of an element.

2) The excess field associated with (*k*,*j*) is:

$$\varepsilon_{k,j}^{(1)} = \max\left[0, u_{k,j}^{n+1,1} - u_{k,j}^{\max}\right] + \min\left[0, u_{k,j}^{n+1,1} - u_{k,j}^{\min}\right] \quad (31)$$

where $u_{k,j}^{n+1,1}$ is the interpolated value at FOCL.

3) Apply a global diffusion operator to ε to obtain estimated velocity at the next iteration:

$$u_{k,j}^{n+1,2} = u_{k,j}^{n+1,1} + \mu' \Delta t \nabla^2 \varepsilon_{k,j}^{(1)}, \ \forall j,k \quad (32)$$

and we use the 5-point filter with maximum strength (cf. (Eqs. (7,28)):

$$u_{k,j}^{n+1,2} = u_{k,j}^{n+1,1} + \frac{1}{8}\left[\varepsilon_{k,1}^{(1)} + \varepsilon_{k,2}^{(1)} + \varepsilon_{k,3}^{(1)} + \varepsilon_{k,4}^{(1)} - 4\varepsilon_{k,j}^{(1)}\right] \quad (33)$$

where subscripts 1-4 are the 4 adjacent sides of *j* (Fig. 5a);

4) Calculate the new excess field using $u_{k,j}^{n+1,2}$ in 2) and apply the filter 3) again to find the velocity at the next iteration $u_{k,j}^{n+1,3}$. Iterate until the excess field falls below a prescribed threshold. In practice, 10 iterations are usually sufficient to bring the excess field below an acceptable level (10^{-4} m/s); the remaining excess field is then further smoothed with the viscosity.

The filter in Eq. (33) is conservative in the sense that it only redistributes excess mass and does not introduce any additional mass. This is similar in spirit to the conservative scheme of Gravel and Staniforth (1994) but appears simpler in implementation. At a boundary side *j*, Eq. (33) is modified in order to maintain the conservation:

$$u_{k,j}^{n+1,2} = u_{k,j}^{n+1,1} + \frac{1}{8}\left[\varepsilon_{k,1}^{(1)} + \varepsilon_{k,2}^{(1)} - 2\varepsilon_{k,j}^{(1)}\right] \quad (34)$$

where subscripts '1' and '2' are the 2 adjacent sides of *j* (Fig. 5d). Note that since the linear interpolation scheme (LI) does not introduce local extrema, ELAD is not applied there.

3.3.1 A convergence test

A combination of filter and higher-order advection schemes is often used in ocean models. Due to the use of filter, the actual order of convergence may be lower than what the original scheme is intended, and should be numerically derived using benchmark tests. As ELM is not a conventional method and direct comparison with upwind-type methods is often lacking in the literature, we demonstrate the order of convergence of various ELM schemes employed in SCHISM using a rotating Gauss hill test. In this test, we fix the advective velocity field as:

$$\begin{cases} u = -\omega y \\ v = \omega x \\ w = 0 \end{cases} \quad (35)$$

with the period of rotation T_0=3000s, and angular frequency $\omega = 2\pi/T_0$. We then use the temperature as a proxy for the velocity; in other words, we define the temperature at side centers and whole levels (just like velocity), convert the side temperature to node temperature, interpolate its value at FOCL, and apply ELAD (for dual kriging ELM) in exactly the same way as we did for velocity. Since we are only concerned with pure advection problem, no viscosity

is applied to the 'temperature'. This way we can study the momentum advection schemes in isolation from other parts of the model. Initially the Gauss hill of unit amplitude is defined as:

$$T = \exp\left[-\frac{(x-x_0)^2 + (y-y_0)^2}{\sigma^2} \right] \tag{36}$$

where x_0=0, y_0=1800m, and σ=850m. We generate a circular grid of radius of 3600m with essentially uniform triangles using DistMesh (Persson and Strang 2004). The side length of triangles is varied in the convergence study as 400m, 200m, 100m, and 50m. The time step used is 300s for Δx=400m and adjusted for other cases such that the Courant number remains constant, and the 2nd-order Runge-Kutta method is used to calculate the characteristic line. For kriging interpolators ('KR'), ELAD is applied with a threshold of 10^{-4} and maximum of 10 iterations (we have also tried a maximum of 100 iterations and the results are similar).

The results with Δx=50m after 1 rotation from various advection schemes are compared with each other and the exact solution in Fig. 6. The two MA schemes have almost no under-/over-shoots (MA-KR3 has a very small undershoot on the order of -10^{-20}), whereas all MB schemes have some dispersion. MB-LI and MB-KR1 have no overshoots, but have undershoots of -2.e-4 and -1.e-4 respectively. On the other hand, MB-KR2 and MB-KR3 lead to much larger overshoots (~0.027; note the distortion near the center of the hill) and smaller undershoots of -4.e-5 and -6.e-5 respectively. These results are an indication of larger numerical diffusion/dissipation inherent in all MA schemes. Note that ELAD is not applied to MB-LI or MA-LI.

The convergence curves from various schemes are summarized in Fig. 7. Highest convergence rate (~1.93) is achieved with MB-KR2 and MB-KR3. However, this is mostly due to the larger errors at coarser resolutions. In terms of RMSE, the best accuracy is achieved with MB-LI followed closely by MB-KR1. The discrepancy between the convergence rate and absolute error as shown here is probably not uncommon in ocean models and has important implications. The leading-order truncation error consists of two parts: a coefficient and an exponential term, and both are equally important. Since the order of convergence is only related to the 2nd part, a 'lower-order' scheme such as MB-LI can still achieve better accuracy if it has a smaller 'coefficient'. While some higher-order methods may theoretically lead to better convergence rate, their accuracy may require an unrealistically fine resolution. Another important consideration is that the use of 'smoothers' in the higher-order methods may also degrade the convergence rate. Despite their relatively lower convergence rates (~1.5), the smaller RMSE and superior shape-preserving ability achieved by MB-LI and MB-KR1 as demonstrated in Figs. 6 &7 make them better choices for practical applications with SCHISM; our experience with many realistic cases also supports the finding here. We therefore use MB-LI for the rest of the paper. However, we should remark that the superior stability of MA schemes makes them ideal for shallow-water environment, and the better accuracy achieved by MA-KR3 may partially mitigate the induced numerical dissipation. Therefore a judicious combination of MA and MB schemes may be ideal for some applications, and this will be explored in future research.

4. Extension to mixed grids

Quads are computationally more economical and in the case of a FEM model like SCHISM, the bilinear shape function associated with quad elements also gives better accuracy than that for triangular elements. Since the ratio between the velocity and elevation spaces becomes smaller with the quad grid, the inertial spurious modes can also be reduced (Danilov and Androsov 2015).

Most schemes in SCHISM are agnostic with respect to element type and therefore their extension to quads is straightforward. The main changes are summarized below. For FEM formulation, bilinear shape function is used for quads, and the integrals are evaluated either analytically or using a 4-point (cubic) Gauss quadrature. Note that the idea of LSC^2 and shaved cell technique can be trivially adapted to quads as well. The changes to TVD^2 are minimal due to the FVM used. Therefore in the following we focus on the new viscosity and ELAD schemes.

For the reason explained in Section 3.2 (i.e. to prevent negative coefficients), we will derive the viscosity form on uniform quads. Referring to Fig. 5b, the viscosity term is:

$$\nabla\cdot(\mu\nabla u)\big|_0 = \frac{\mu_0}{A_I + A_{II}}\left[\left(\frac{\partial u}{\partial n}\right)_1 + \left(\frac{\partial u}{\partial n}\right)_2 + \left(\frac{\partial u}{\partial n}\right)_3 + \left(\frac{\partial u}{\partial n}\right)_4 + \left(\frac{\partial u}{\partial n}\right)_5 + \left(\frac{\partial u}{\partial n}\right)_6 \right] \tag{37}$$

And the normal derivatives are evaluated inside the 2 smaller squares formed by the dashed lines. For convenience we rotate the coordinate frame so that the *x*- and *y*-axes are perpendicular to lines (0,1) and (1,2) respectively and the origin is located at the center of element *I* (note that the viscosity term is invariant under coordinate rotation). The transformation from (x,y) to local coordinates (υ,ξ) is then simply: $x=b\upsilon$ and $y=b\xi$, where $b=\sqrt{2}a/4$ and a is the element side length. The 4 shape functions associated with points 0,1,2,3 are:

$$\varphi_i(x,y)=\frac{1}{4}\left(1+\xi_i\frac{x}{b}\right)\left(1+\upsilon_i\frac{y}{b}\right),\ (i=1,..,4) \tag{38}$$

where $|\xi_i|=|\upsilon_i|=1$ are the local coordinates of the 4 points. Unlike in the case of triangles, the derivatives of u are no longer constant within each square but need to be evaluated using the derivatives of the shape functions (38). The final form is:

$$\nabla\cdot(\mu\nabla u)\big|_0=\gamma_4\left(u_1+u_3+u_4+u_6-4u_0\right) \tag{39}$$

where $\gamma_4=\mu_0/(2a^2)$. Note the absence of points 2 and 5 here. Eq. (39) is analogous to the traditional 5-point Laplacian operator for structured-grids and also to the 5-point viscosity for the triangles Eq. (28). Therefore the viscosity for a mixed grid involves only the 4 nearest adjacent sides, regardless of whether the element is triangular or quadrangular. The bi-harmonic viscosity for mixed triangular-quadrangular elements can be readily derived using Eq. (39) and the first half of Eq. (29). Since the ELAD operator is built on the Laplacian viscosity, Eqs. (33,34) can be easily extended to include quad elements as well.

The combination of LSC^2 vertical grid (Zhang et al. 2015) and horizontal mixed-element grids results in an extremely flexible grid system that has great practical applications. We demonstrate this with a toy problem for coastal ocean-estuary-river system depicted in Fig. 8. Since the tracer concentrations are defined at the prism centers, a row of quads and 1 vertical layer resembles a 1D model (Fig. 8c). Similarly, a row of quads with multiple vertical layers leads to 2DV configuration (Fig. 8c). Some parts of the shoals that are sufficiently shallow are discretized using 1 vertical layer (Fig. 8b), which is a 2DH configuration. The deeper part of the domain is discretized using full 3D prisms, but with a larger number of layers in the deeper depths than in the shallow depths, in a typical LSC^2 fashion (Fig. 8a; Zhang et al. 2015). Different types of grids are *seamlessly* welded into a *single* SCHISM grid, resulting in greatest efficiency. With some care taken of the consistent bottom friction formulations across 1D, 2D and 3D (we used a constant drag coefficient of 0.0025 here), the model results show no discontinuity across different types of grids (Fig. 9). The use of 1D or 2D cells in shallow areas also enhances numerical stability, as they are well suited and more stable for inundation process than 3D cells; e.g., the crowding of multiple 3D layers in the shallow depths is not conducive to stability.

5. Numerical experiments

The SCHISM model, with the new developments detailed in previous sections, has been successfully applied by Ye et al. (submitted) to the Chesapeake Bay, by Zhang et al. (2016) to North Sea-Baltic Sea system, and by Stanev et al. (in preparation) to the Black Sea-Turkish Straits system. Here we will focus on benchmarking its performance in the eddying regime, which is the last missing link for our cross-scale model. The 1st case is a simple lock exchange experiment that has been previously used for inter-model assessment. The 2nd case deals with baroclinic instability in a zonally re-entrant channel, and the 3rd case is focused on mesoscale eddies and meanders in the Black Sea. We conclude this section with a brief discussion on the strategy for cross-scale applications.

5.1 Lock exchange test

Ilicak et al. (2012) assessed the spurious dianeutral mixing in 4 structured-grid models through 5 tests, and found that the amount of spurious dianeutral mixing is proportional to the grid Reynolds number and is also influenced by the viscosity.

Their 1st is a simple lock exchange experiment, for which theoretical results for the propagation speed of the gravity current are available (Benjamin 1968). They presented model results from various horizontal and vertical resolutions and used an isopycnal-coordinate model (GOLD) as benchmark. In addition they suggest that the reference potential energy can be used as an effective tool to detect spurious dianeutral mixing.

Here we use as close a model set-up to their 1st test as possible in order to help assess the relative performance of SCHISM for this test. The domain is 64km long with a constant depth of 20m and initially each of two water masses of 5°C and 35°C occupies half of the domain. A linear equation of state is used where the water density is linearly dependent on the temperature alone. A main difference in our model set-up is that a larger time step (200s) is used in SCHISM, as it is an implicit model.

We conduct convergence study with respect to horizontal and vertical grid resolution as in Ilicak et al. (2012). For simplicity uniform horizontal grids and uniform σ layers are used. Fig. 10(a-d) shows the temperature snapshots from refining the vertical grid. In comparison to Figs. 1 and 2 of Ilicak et al. (2012), we remark that SCHISM results show less noise (using GOLD results as benchmark) especially at higher resolution. The high-resolution SCHISM results also show a thinner pycnocline compared to some of the other models, suggesting acceptable amount of numerical dissipation. We have also used two smaller time steps (Δt=150s, 100s) to further test the model sensitivity, and Fig. 10(e&f) reveals only some subtle differences, mostly in the form of a smaller propagation speed of the fronts than that from Δt=200s (Fig. 10d). Decreasing the time step further would eventually degrade the model skill as the CFL number becomes too small (Zhang et al. 2015).

The predicted front locations from different horizontal and vertical resolutions are illustrated in Fig. 11ab. With the exception of the coarsest vertical resolution (2 layers), SCHISM results compare favorably with other models, especially at the highest resolution (with the error within 1% of the theoretical value) (Fig. 11a). With the exception of the coarsest horizontal resolution (4km), the model results show only small sensitivity to the horizontal resolution (Fig. 11b). The model's accuracy, convergence and low inherent dissipation are well demonstrated for this baroclinic test.

5.2 Reentrant channel

Danilov (2012) and Danilov and Wang (private communication) used this case to demonstrate the 'geometric' issues associated with various types of grid-variable arrangements. The domain is essentially a zonal band occupying between 30°N and 45°N. Since periodic boundary condition, which is required if we were to use their smaller domain (20° to 40° long in the zonal direction), is not available in SCHISM, here we use the entire zonal band (from 180°W to 180°E), which results in a much larger grid. Note that a quasi-periodic solution is expected for the larger domain (cf. Fig. 13).

Initially the salinity is constant at 35PSU (and remains so throughout the simulation), and there is a linear gradient of temperature along the meridional and vertical directions. In addition, a small amount of 'noise' is added to the initial temperature along the zonal direction in order to speed up the development of baroclinic instability (Danilov 2012). Therefore the initial temperature is given as:

$$T(t=0) = 25 + \alpha_1 z + \alpha_2(\varphi - \varphi_0) + \alpha_3 \cos(2\pi\lambda / L_0) \qquad (40)$$

where α_1=8.2x10^{-3} °C/m, α_2=–0.5566 °C/(degree latitude), α_3=0.01°C, L_0=20°, φ is the latitude, φ_0 =30°N, and λ is the longitude. The flow is forced by relaxing temperature to its initial distributions in two 1.5°-wide southern and northern relaxation zones near the boundary, with the relaxation scale linearly decreasing from 3 days to zero within these zones. The bottom drag coefficient is kept constant at 0.0025.

In the SCHISM set-up, we use the spherical coordinate option implemented with local coordinate frame transformations (Comblen et al. 2009) and the same resolution as in Danilov (2012): 1/7° along zonal and 1/6° along meridional directions. In the vertical dimension we use 24 *S* levels to cover the (constant) 1600m depth, with spacing constants of h_c=30m, θ_b=0, θ_f=5 in order to better resolve the surface layers. We use a time step of 300s, and a bi-harmonic viscosity (see Section 3). No explicit horizontal diffusivity is used and the vertical viscosity and diffusivity are calculated from the generic length-scale model with a *k-kl* configuration (implemented from the formulation of Umlauf and Burchard (2003)). The horizontal grid has 229K nodes, and the simulation runs ~200 times faster than real time on 216 Intel Xeon cores.

Eddies and filaments develop quickly within 0.5 years, and the mean kinetic energy (MKE) reaches a quasi-steady level after ~1 year (Fig. 12). The maximum MKE from SCHISM (~0.07 m^2/s^2) seems to be close to the scheme MC (~0.07 m^2/s^2) but smaller than A-grid (~0.1 m^2/s^2) of Danilov (2012); the amplitude of oscillation is also smaller. The snapshots of Sea-Surface Height (SSH) shows certain periodicity along the zonal band but the wavelength is shorter than that used in the initial noise (i.e. 20°; Eq. (40)) (Fig. 13). To facilitate qualitative comparison with Danilov (2012) and Danilov and Wang (private communication), snapshots, in a 30° zonal band, of SSH and temperature and vortcitiy

at 100m depth are presented in Fig. 14. Qualitatively similar looking eddies and filaments structures are evident in this figure, although our temperature is slightly lower (Fig. 14b). Our filaments also seem to be a little shorter than their best results (Danilov 2012), suggesting slightly larger numerical dissipation in our model. The differences between our and their results may also be partly due to the larger domain we have used.

5.3 Black Sea

The Black Sea, our realistic-model laboratory used in this study to validate the outcome of the numerical methods proposed here, is a nearly enclosed basin of estuarine type (Fig. 15). The run-off from its catchment area (about five times the basin area) is large (10000-20000m^3/s) relative to the basin volume (5.4×10^5 km^3). The sea is connected with the Mediterranean Sea through the Turkish Straits System (the Bosphorus Strait, the Sea of Marmara and the Dardanelles Strait). Because the straits are very narrow and shallow the Black Sea is almost completely isolated from world's ocean (Özsoy and Ünlüata 1997; Stanev 2005; Stanev and Lu 2013). The large freshwater flux and the small water exchange with the Mediterranean support a distinct vertical layering limiting the vertical exchange and create a unique chemical and biological environment (the Black Sea is the worlds' largest anoxic basin). Thus this sea can be considered as a natural playground to study geophysical hydrodynamics in the presence of pronounced vertical stratification (salinity changes from ~18PSU at sea surface to ~21PSU at 180 m depth).

The Black Sea is a deep estuarine basin. The continental slope in the Black Sea is very variable (Fig. 15b). It is mild in the north-western part, very steep in the southern and eastern part and is carved by deep canyons along the southern coast. This natural setting is also very favorable to study the interaction between stratification and topography as well as the role of planetary and topographic beta-effects (Stanev and Staneva 2000). This interplay results in a general circulation that follows the continental slope and is usually structured in two connected gyre systems encompassing the basin (the Rim Current). This jet-current system is associated with a difference of ~0.2 m between sea levels in the coastal and open sea, with seasonal amplitudes of ~10 to 20 cm, and inter-annual variations of ~5 to 10 cm (Stanev and Peneva 2002).

A comprehensive presentation of SCHISM results for the Black Sea-Turkish Strait System (BS-TSS) is beyond the scope of this paper and has been reported elsewhere (Stanev et al., in preparation). Here we will only focus on assessing the model performance in the eddying regime in the Black Sea. The main DEM source we used is from the GEBCO Digital Atlas (IOC, IHO and BODC 2003). To initialize the model, we use a monthly climatology of salinity and temperature for Black Sea. The 0.2° ECMWF product is used for atmospheric forcings: wind, atmospheric pressure, and air temperature. The 36-km CFSR product (http://rda.ucar.edu/datasets/ds093.1/, last accessed Sept. 17 2015) is used for heat and precipitation fluxes due to the lack thereof in the ECMWF product. Discharges at 6 rivers around Black Sea (Fig. 15a) are from monthly mean values, and the (constant) long-term mean flows are used for the 2 major rivers in Azov Sea (Kuban and Don). The excess river flow is compensated by an equivalent outflow through the Bosporus Straits.

We generate a mixed triangular-quadrangular grid of 101K nodes and 172 K element (Fig. 15d). An essentially uniform resolution of 3km is used here to exclude the influence of variable grid resolution on mesoscale processes (see Danilov and Wang (2015) for a detailed discussion on the effects of variable grid resolution on eddies). The refinement near the Bosphorus exit is done for the on-going work that includes the Turkish Strait System. Once the model is fully validated on this grid, we plan to create an UG of variable resolution to refine some coastal areas. Even though the bottom slope is very steep at the shelf break, *no* bathymetry smoothing is done to stabilize the model. A measure of 'hydrostatic consistency' (Haney 1991) is given by the Hannah-Wright ratio, defined as $|\Delta h/h_{min}|$, where. h_{min} is the minimum depth in an element, and Δh is the maximum difference of depths at nodes in the element (Hannah and Wright 1995). An upper limit of 0.1 for this ratio is usually recommended for terrain-following coordinate models, but Fig. 15c indicates that the ratio is generally much larger than this threshold near the shelf break. We use a LSC^2 grid in the vertical, with maximum of 53 levels (in the deepest part of Black Sea) and average of 35.4 levels. The time step is set at 120s, and a constant 0.5mm bottom roughness is used. The same bi-harmonic viscosity and vertical viscosity/diffusivity schemes as in Section 5.2 are used here. The model runs 130 times faster than real time on 144 CPUs. In contrast, the real-time ratio is reduced to 50 with the explicit TVD method.

Fig. 16a shows a typical progression of eddies and meanders inside Black Sea. The Rim Current is accompanied by a series of eddies on both sides, with the anticyclonic mesoscale eddies located between the continental slope and the coast. Their typical radius is between 50 and 100 km as determined by internal radius of deformation. Growing in size some of them detach and propagate into the open sea, e.g., the eddy that is displaced from the south-eastern coastal

area and stagnated along the Caucasian coast. Sub-basin scale eddies such as Batumi and Sevastopol eddies, which are the well-known representatives of vorticity field (Stanev et al. 2000), are also well replicated by the model. Because the transition between summer (less organized) and winter (almost one-gyre) circulation is controlled by the baroclinic eddies (Stanev and Staneva 2000), the present simulation by SCHISM that resolves well the eddy variability has a potential to successfully treat these basic aspects of seasonal evolution.

The patterns of sea surface shown every 5th day agree well with earlier numerical simulations using structured-grid models (Stanev 2005). The number of coastal anticyclones of about 8 compares well with the number of observed ones, which is derived from the statistics using SSALTO/ DUACS data product (http://www.aviso.altimetry.fr/en/data/product-information/information-about-mono-and-multi-mission-processing/ssaltoduacs-multimission-altimeter-products.html; last accessed Jan 29, 2016). Similarly to those previous results, the meandering activity is especially intense near steeper slopes, e.g. in the northern, eastern and southern coasts. The loop current and eastern and western gyres in the middle of the basin are clearly visible.

The model's ability to resolve the baroclinic instability is contrasted below with SELFE results using the same initial data and forcing, and a similar horizontal and vertical resolution (21*S*+30*Z* layers) (Fig. 16b); the SELFE results represented the best we were able to obtain from this model. There are apparent similarities between the two models: the shape of the cyclonic gyre in the middle is similar, and the contrast of sea levels between coastal and open sea is comparable, although the eddy-resolving SCHISM simulation shows a steeper sea-surface slope. The performance of the two models in the area of the shallow Azov Sea, where the process is mostly driven by propagating atmospheric disturbances and dominated by friction, is also similar. However a number of major differences between the two models are apparent, and the most pronounced among them is the clockwise circulation in the eastern-most part of the Black Sea predicted by SELFE versus the formation of an eddy dipole in SCHISM. SELFE is also not in a position to adequately simulate the counter-current along the west coast, which is commonly observed in this area; the well-known Sebastopol eddy is totally missing in this model as well. A number of smaller eddies in the north and south coasts are also successfully captured by SCHISM but not by SELFE. The smoother SSH produced by SELFE is mostly a symptom of the larger dissipation inherent in the model, although the lack of LSC^2 grid therein is also partially responsible (SCHISM results with the same *SZ* grid indicate only mild degradation of model skill; not shown). Since SELFE does not have implicit TVD^2 solver, its efficiency for this case is similar to SCHISM with the explicit TVD method.

Differences in the surface heights associated with these eddies between SELFE and SCHISM are 5-10 cm, which is comparable to the anomalies caused by eddies (Stanev et al. 2000). Therefore we conclude that SELFE filters out baroclinic instability, especially eddies with diameter of about 100 km, which are the characteristic scales of eddies seen in altimeter, drifter and color data (Ozsoy et al. 1993; Stanev 2005). The meanders predicted by SCHISM on the Rim Current propagate with a speed of about 20 cm/s, and in some specific areas, such as the area east of Sakarya Canyon (29-31 E), the propagation speed often exceeds 1 m/s. These are also consistent with the observations (Ozsoy et al. 1993).

5.4 Outlook: from creek to ocean

The satisfactory performance of SCHISM in the eddying regime as demonstrated in the previous test cases, and in the non-eddying regime as demonstrated previously, makes it potentially capable of seamlessly simulating processes from deep ocean to shallow environment in estuaries, rivers, creeks and lakes. We remark that the time step we used for the realistic field case of Black Sea, North Sea-Baltic Sea (Zhang et al. 2016) and Kuroshio (Zhang et al. 2015) falls in the same range as that for the non-eddying regime, i.e. 100-200sec, and therefore a single time step can be used for cross-scale applications. Our experience so far demonstrates that as long as one pays attention to smooth transition of grid resolution from eddying to non-eddying regimes, and adds back some numerical dissipation in the non-eddying regime (e.g. via a larger viscosity locally or filter), SCHISM is capable of simulating creek-to-ocean system as a whole without the need for grid nesting. Demonstration of such a seamless capability is on-going for BS-TSS, South and East China Seas, and US east coast and will be reported in upcoming publications.

6. Conclusions

We have developed a new cross-scale unstructured-grid model (SCHISM) by revamping key formulations in an older model (SELFE). Major revisions include: (1) a new implicit transport solver (TVD^2) using 2 limiter functions (in space and in time), which has been demonstrated to be accurate and efficient for a wide range of Courant numbers; (2) a new horizontal viscosity formulation for generic unstructured grids; (3) a new higher-order scheme for

momentum advection coupled with an iterative smoother to reduce excess mass; (4) addition of quad elements, which in conjunction with the flexible vertical grid system used in SCHISM leads to an advantageous polymorphism (with 1D/2DV/2DH/3D cells being unified in a single model grid).

These new revisions prove crucial in SCHISM's capability in successfully simulating processes in the eddying regime, as demonstrated by the results from the 2 challenging test cases, mainly due to the much reduced numerical dissipation and enhanced efficiency. Recently the seamless cross-scale capability of SCHISM has also been successfully tested with several other applications..

Ongoing work focuses on some transitional issues between eddying and non-eddying regimes as well as enabling variable resolution in the eddying regime. Our and other's experience (Danilov, private communication) suggests that numerical schemes designed for eddying regime may not be ideal for non-eddying regime, and therefore transition of schemes might be desirable. In our case, the combination of MB-LI and MA-KR3 holds most promise, as the latter is ideal for shallow and inundation processes.

Acknowledgements

The first author thanks Dr. Sergey Danilov for many enlightening discussions on the subject of eddying regime. Part of this work was accomplished during the 1st author's tenure as a HWK Fellow and financial support by Hanse-Wissenschaftskolleg (HWK, Germany) is gratefully acknowledged. S. Grashorn is funded by the initiative Earth Science Knowledge Platform (ESKP) operated by the Helmholtz Association. Simulations shown in this paper were conducted on the following HPC resources: (1) Sciclone at the College of William and Mary which were provided with the assistance of the National Science Foundation, the Virginia Port Authority, and Virginia's Commonwealth Technology Research Fund; (2) the Extreme Science and Engineering Discovery Environment (XSEDE; Grant TG-OCE130032), which is supported by National Science Foundation grant number OCI-1053575; (3) NASA's Pleiades. The authors thank the comments made by 3 anonymous reviewers which made the paper stronger.

Figure captions

Fig. 1: SCHISM modelling system. The modules that are linked by arrows can exchange internal data directly without going through the hydrodynamic core in the center.

Fig. 2: Staggering of variables in SELFE/SCHISM. The elevation is defined at node (vertex) of a triangular element, horizontal velocity at side center and whole levels, vertical velocity at element centroid and whole level, and tracers at the prism center. The variable arrangement on a quad prism in SCHISM is similar. The top and bottom faces of the prism may not be horizontal, but the other 3 faces are always vertical.

Fig. 3: Two steps in Eulerian-Lagrangian method. (a) The characteristic equation (6) is integrated backward in space and time, starting from a side center (the green dot). The characteristic line is further subdivided into smaller intervals (bounded by the red dots), based on local flow gradients, and a 2nd-order Runge-Kutta method is used within each interval. The foot of characteristic line is marked as a yellow dot. Note that the vertical position of the trajectory is also changing and so the tracking is in 3D space. (b) Interpolation is carried out at FOCL (yellow dot), based on either the nodes of the containing elements (blue dots), or the 2-tier neighborhood (blue plus red dots; the latter are the neighbors of the blue dots) using a dual kriging method. Proper linear vertical interpolation has been carried out first to bring the values at each node onto a horizontal plane before the horizontal interpolation is done.

Fig. 4: Two methods of converting side velocities to a node velocity. (a) Inverse distance interpolation from sides (blue dots) to node (yellow dot); (b) use of FEM shape function to find the node velocity within each element first (the red arrow), i.e. $\mathbf{u}_1=\mathbf{u}_{II}+\mathbf{u}_{III}-\mathbf{u}_I$, followed by a simple averaging method to calculate the final value from all of its surrounding elements (dashed arrows).

Fig. 5: Shapiro filters for (a) triangular and (b) quadrangular elements. The same stencils are used to construct the viscosity. '*I*' and '*II*' are 2 adjacent elements of side of interest ('0'). The extended stencil used in constructing bi-harmonic viscosity is shown in (c). The special case of a boundary side is shown in (d).

Fig. 6: Temperature after 1 rotation in the rotating Gauss hill test from various schemes with Δx=50m. ELAD filter is applied to all 'KR' schemes.

Fig. 7: Convergence curves of various advection schemes. The equations in each panel are linear regression fit. The intersection with *x*-axis in each equation is related to the coefficient of leading-order truncation error, and MB-LI has the smallest value.

Fig. 8: Model polymorphism illustrated with a toy problem. The mixed triangular-quadrangular grid and the bathymetry are shown in the foreground. The vertical transect grid along the redline going from deep ocean into estuary ('shipping channel') is shown in insert (a). The 3D view of the grid near the head of estuary is shown in insert (b), with few layers on the shallow shoals. The grid near the upstream river is shown in insert (c), where transition from 2DV to 1D grid can be seen. In the test, a M2 tide is applied at the ocean boundary, and fresh water discharges are imposed at the heads of the river and estuary.

Fig. 9: Snapshot of velocity (a&c) and salinity (b&d) along the river transect (cf. Fig. 8c) showing the transition from 2DV to 1D region (i.e. the flat portion on the left). (a&b) correspond to a peak flood and (c&d) a peak ebb. The uni-directional river flow can be seen even during flood, and the tilt of isohaline line in (b) into the 1D zone is due to the linear interpolation of colors used in plotting; otherwise the 1D zone shows a uniform salinity/velocity along the vertical column. The burgundy line in (a&c) is the bottom.

Fig. 10: Vertical transects of temperature at t=17 hours, with vertical resolution of 10, 5, 2 and 1m, and two different time steps (e&f). The horizontal resolution is fixed at 500m.

Fig. 11: Time history of front location from (a) different vertical resolution (with horizontal resolution fixed at 500m); (b) different horizontal resolution (with vertical resolution fixed at 1m). The time step is fixed at 200s. The theoretical results of Benjamin (1968) are also shown.

Fig. 12: Simulated mean kinetic energy (doubled kinetic energy scaled by mass) over time.

Fig. 13: Snapshot of SSH for the entire grid showing periodicity along the zonal band.

Fig. 14: Snapshot of (a) SSH, (b) temperature at 100m depth, and (c) relative vorticity (scaled by local Coriolis parameter) at 100m depth.

Fig. 15: (a) Black Sea bathymetry. Also shown are major geographic names and rivers around Black Sea (Sakarya, Kizilirmak, Rioni, Dniepr, Dniestr, and Danube) and Azov Sea (Don and Kubon). (b) Bottom slope ($\sqrt{(\partial h/\partial x)^2 + (\partial h/\partial y)^2}$) of Black Sea, with values larger than 0.05 (1:20) being highlighted. (c) Hannah-Wright ratios, with values larger than 0.1 being highlighted. (d) SCHISM grid for Black Sea showing the placement of nodes. Uniform resolution of 3km is used except near the exit to Bosphorus Strait.

Fig. 16: Snapshots of SSH from (a) SCHISM; (b) SELFE. The time stamps are shown near the top of each panel. Major eddies in Black Sea can be seen in (a) and compared with Stanev (2005).

REFERENCES

Arakawa, A. and V.R. Lamb (1977) Computational design of the basic dynamical processes of the UCLA general circulation model, Methods of Computational Physics 17. New York: Academic Press. pp. 173–265.

Azevedo, A., Oliveira, A., Fortunato, A.B., Zhang, Y. and A.M. Baptista (2014) A cross-scale numerical modeling system for management support of oil spill accidents, Marine Pollution Bulletin, 80, 132-147.

Benjamin, T.B. (1968) Gravity currents and related phenomena. J. Fluid Mech. 31, 209–248.

Bertin, X., Li, K., Roland, A., Zhang, Y., Breilh, J.F. and E. Chaumillon (2014), A modeling-based analysis of the flooding associated with Xynthia, central Bay of Biscay, Ocean Eng, 94, 80-89.

Burla, M., Baptista, A.M. Zhang, Y., and S. Frolov (2010), Seasonal and inter-annual variability of the Columbia River plume: a perspective enabled by multi-year simulation databases. Journal of Geophysical Research: special issue on NSF RISE project, 115, C00B16.

Casulli, V. and E. Cattani (1994), Stability, accuracy and efficiency of a semiimplicit method for 3D shallow water flow, Comput. Math. Appl., 27, 99–112.

Casulli, V. and P. Zanolli (2005), High resolution methods for multidimensional advection–diffusion problems in free-surface hydrodynamics, Ocean Model., 10, 137–151.

731 Cerco, C. and T. Cole (1993), Three-Dimensional Eutrophication Model of Chesapeake Bay. J. Environ. Eng., 119(6),
732 1006–1025.

733 Chai, F., Dugdale, R.C., Peng, T-H, Wilkerson, F.P. and R. T. Barber (2002), One Dimensional Ecosystem Model of
734 the Equatorial Pacific Upwelling System, Part I: Model Development and Silicon and Nitrogen Cycle. Deep-Sea Res.
735 II,. 49(13-14), 2713-2745.

736 Comblen, R., Legrand, S., Deleersnijder E., and V. Legat (2009), A finite element method for solving the shallow
737 water equations on the sphere. Ocean Modelling, 28, 12-23.

738 Cotter, C.J., Ham, D.A. (2011) Numerical wave propagation for the triangular P1DG-P2 finite element pair, J.
739 Comput. Phys., 230, 2806-2820.
740 Danilov, S. (2012), Two finite-volume unstructured mesh models for large-scale ocean modeling, Ocean Modelling
741 47, 14–25.

742 Danilov, S. and A. Androsov (2015), Cell-vertex discretization of shallow water equations on mixed unstructured
743 meshes, Ocean Dyn. 65, 33–47.

744 Danilov, S. and Q. Wang (2015), Resolving eddies by local mesh refinement, Ocean Modelling, 93, 75-83.

745 Danilov, S. and Q. Wang (private communication) Resolving eddies by local mesh refinement.

746 Dodet, G. (2013), Morphodynamic modelling of a wave-dominated tidal inlet: the Albufeira Lagoon, Ph.D. thesis,
747 Univ. La Rochelle (France).

748 Duraisamy, K. and J.D. Baeder (2007), Implicit Scheme For Hyperbolic Conservation Laws Using Nonoscillatory
749 Reconstruction In Space And Time, Siam J. Sci. Comput. 29(6), 2607–2620.

750 Griffies, S.M. and R.W. Hallberg (2000), Biharmonic Friction with a Smagorinsky-Like Viscosity for Use in Large-
751 Scale Eddy-Permitting Ocean Models, Monthly Weather Review, 128, 2935-46.

752 Gravel, S. and A. Staniforth (1994), A mass-conserving semi-Lagrangian scheme for the shallow-water equations,
753 Mon. Wea. Rev., 122, 243-248.

754 Ham, D.A., Pietrzak, J., and G.S. Stelling (2006), A streamline tracking algorithm for semi-Lagrangian advection
755 schemes based on the analytic integration of the velocity field, Journal of Computational and Applied Mathematics
756 192, 168–174.

757 Ham, D.A., Kramer, S.C., Stelling, G.S., and J. Pietrzak (2007), The symmetry and stability of unstructured mesh C-
758 grid shallow water models under the influence of Coriolis, Ocean Modelling 16, 47–60.

759 Haney, R.L. (1991) On the pressure gradient force over steep topography in sigma coordinate ocean models, J.

760 Phys. Oceanogr., 21, 610–619.

761 Hannah C. G., and D. G. Wright (1995), Depth dependent analytical and numerical solutions for wind-driven flow
762 in the coastal ocean, Quantitative Skill Assessment for Coastal Ocean Models. D. R. Lynch and A. M. Davies (Ed.),
763 A.G.U. 47, 125-152.

764 Ilicak, M., Adcroft, A.J., Griffies, S. M., and R.W. Hallberg (2012), Spurious dianeutral mixing and the role of
765 momentum closure. Ocean Modelling, 45-46(0):37-58.

766 Le Roux, D.Y., Lin, C.A., Staniforth, A. (1997), An accurate interpolating scheme for semi-Lagrangian advection on
767 an unstructured mesh for ocean modelling, Tellus, 49A, 119–138.

768 Le Roux, D.Y., Sène, A., Rostand, V., and E. Hanert (2005), On some spurious mode issues in shallow-water models
769 using a linear algebra approach. Ocean Modelling 10, 83–94.

770 Le Roux, D.Y. (2012) Spurious inertial oscillations in shallow-water models, J. Comput. Phys. 231, 7959-7987.

771 IOC, IHO and BODC (2003), Centenary Edition of the GEBCO Digital Atlas, published on CD-ROM on behalf of
772 the Intergovernmental Oceanographic Commission and the International Hydrographic Organization as part of the
773 General Bathymetric Chart of the Oceans, British Oceanographic Data Centre, Liverpool, U.K.

Özsoy E., Ünlüata Ü. and Top Z. (1993), The evolution of Mediterranean water in the Black Sea: interior mixing and material transport by double diffusive intrusions. Progress In Oceanography, 31, 3, 275–320.

Özsoy, E. and Ü. Ünlüata (1997), Oceanography of the Black Sea: A Review of Some Recent Results, Earth Sci. Rev., 42(4), 231-272.

Persson, P. and G. Strang, (2004) A Simple Mesh Generator in MATLAB, SIAM Review, 46(2), 329-345.

Pinto, L., Fortunato, A.B., Zhang, Y., Oliveira, A. and F.E.P.Sancho (2012), Development and validation of a three-dimensional morphodynamic modelling system, Ocean Modelling, 57-58, 1-14.

Ringler, T.D., Thuburn, J., Klemp, J.B., and W.C. Skamarock (2010), A unified approach to energy conservation and potential vorticity dynamics for arbitrarily-structured C-grids, J. Comput. Phys. 229, 3065–3090.

Rodrigues M., A. Oliveira, H. Queiroga, A.B. Fortunato, and Y. Zhang (2009), Three-dimensional modeling of the lower trophic levels in the Ria de Aveiro (Portugal), Ecological Modelling, 220(9-10), 1274-1290.

Roland, A., Zhang, Y., Wang, H.V., Meng, Y., Teng, Y., Maderich, V., Brovchenko, I., Dutour-Sikiric, M. and U. Zanke (2012), A fully coupled wave-current model on unstructured grids, Journal of Geophysical Research-Oceans,117,C00J33,doi:10.1029/2012JC007952.

Shapiro, R. (1970), Smoothing, filtering and boundary effects, Rev. Geophys. Space Phys. 8 (2), 359–387.

Shchepetkin, A.F. and J.C. Mcwilliams (1998), Quasi-Monotone Advection Schemes Based on Explicit Locally Adaptive Dissipation , Monthly Weather Review, 126, 1541-80.

Shen, J. and L. Haas (2004) Calculating age and residence time in the tidal York River using three-dimensional model experiments, Estuarine, Coastal and Shelf Science, 61, 449–461.

Stanev, E.V. and J.V. Staneva (2000), The impact of the baroclinic eddies and basin oscillations on the transitions between different quasi-stable states of the Black Sea circulation, Journal of Marine Systems 24:3-26.

Stanev, E.V., Le Traon, P.-Y., E.L., Peneva (2000), Sea level variations and their dependency on meteorological and hydrological forcing. Analysis of altimeter and surface data for the Black Sea. J. Geophys. Res., vol. 105 (C7), 17203–17216.

Stanev, E.V, and E.L. Peneva (2002), Regional sea level response to global climatic change: Black Sea examples, Glob Planet Change, 32, 33–47

Stanev, E.V. (2005), Understanding Black Sea Dynamics: Overview of recent numerical modelling. Oceanography, 18 (2), 52–71.

Stanev, E.V. and X. Lu (2013), European semi-enclosed seas: basic physical processes and their numerical modelling. In: Soomere,T., Quak,E.(Eds.), Preventive methods for coastal protection. Springer, Switzerland, pp.131–179. doi:10.1007/978-3-319-00440-2_5.

Stanev, E.V., Grashorn, S. and Y. Zhang (in preparation) Cascading estuaries: Numerical simulations of the Inter-basin exchange in the coupled Azov-Black-Marmara-Medirerranean Seas system, Ocean Modelling.

Umlauf, L. and H. Burchard (2003), A generic length-scale equation for geophysical turbulence models, J. Mar. Res. 6, 235–265.

Ye, F., Zhang, Y., Friedrichs, M., Irby, I., Shen, J., Wang, H.V., and Z. Wang (submitted) A 3D baroclinic model of the upper Chesapeake Bay and its tributaries, Ocean Modelling.

Zanke, U.C.E. (2003), On the influence of turbulence on the initiation of sediment motion. International Journal of Sediment Research, 18(1), 17.

Zhang, Y., Baptista, A.M., and E.P. Myers (2004), A cross-scale model for 3D baroclinic circulation in estuary–plume–shelf systems: I. Formulation and skill assessment. Cont. Shelf Res., 24, 2187–2214.

Zhang, Y., and A. M. Baptista (2008), SELFE: A semi-implicit Eulerian–Lagrangian finite-element model for cross-scale ocean circulation, Ocean Modelling, 21(3–4), 71-96.

Zhang, Y., R.C. Witter, and G.R. Priest (2011), Tsunami–tide interaction in 1964 Prince William Sound tsunami, Ocean Modelling, 40(3–4), 246-259.

819 Zhang, Y., Ateljevich, E., Yu, H-C., Wu, C-H., and J.C.S. Yu (2015), A new vertical coordinate system for a 3D
820 unstructured-grid model, Ocean Modelling, 85, 16-31.

821 Zhang, Y., Stanev, E.V. and S. Grashorn (2016) Unstructured-grid model for the North Sea and Baltic Sea: validation
822 against observations, Ocean Modelling, 97, 91-108.

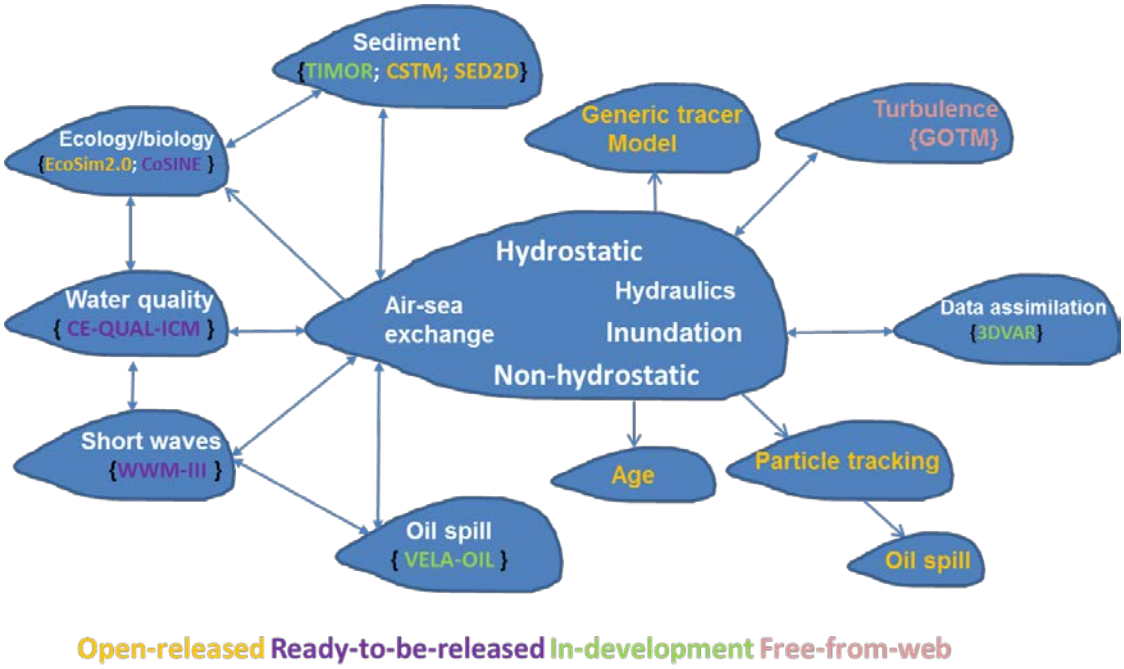

Fig. 1: SCHISM modelling system. The modules that are linked by arrows can exchange internal data directly without going through the hydrodynamic core in the center.

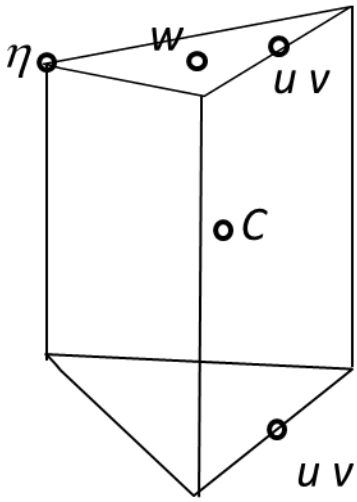

Fig. 2: Staggering of variables in SELFE/SCHISM. The elevation is defined at node (vertex) of an element, horizontal velocity at side center and whole levels, vertical velocity at element centroid and whole level, and tracers at the prism center. The variable arrangement on a quad prism in SCHISM is similar. The top and bottom faces of the prism may not be horizontal, but the other 3 faces are always vertical.

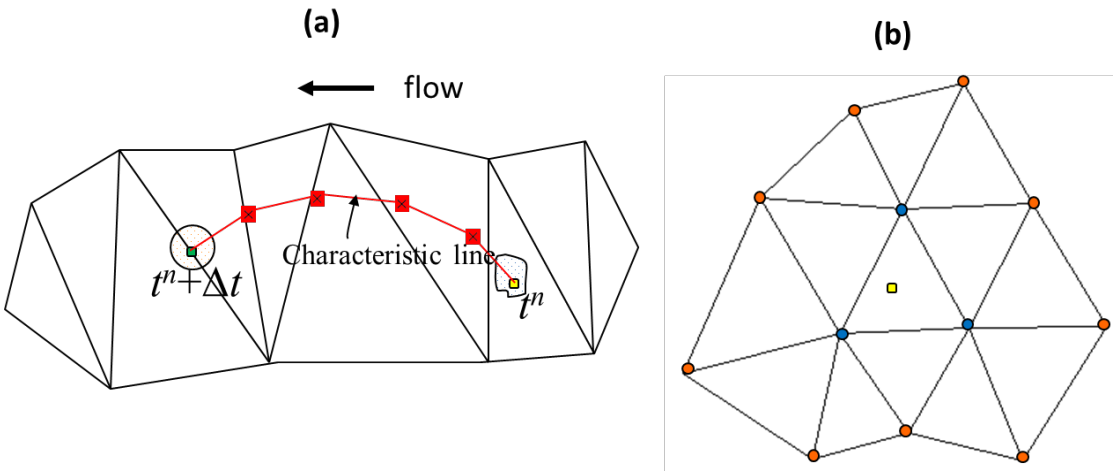

Fig. 3: Two steps in Eulerian-Lagrangian method. (a) The characteristic equation (6) is integrated backward in space and time, starting from a side center (the green dot). The characteristic line is further subdivided into smaller intervals (bounded by the red dots), based on local flow gradients, and a 2nd-order Runge-Kutta method is used within each interval. The foot of characteristic line is marked as a yellow dot. Note that the vertical position of the trajectory is also changing and so the tracking is in 3D space. (b) Interpolation is carried out at FOCL (yellow dot), based on either the nodes of the containing elements (blue dots), or the 2-tier neighborhood (blue plus red dots; the latter are the neighbors of the blue dots) using a dual kriging method. Proper vertical interpolation has been carried out first to bring the values at each node onto a horizontal plane before the horizontal interpolation is done.

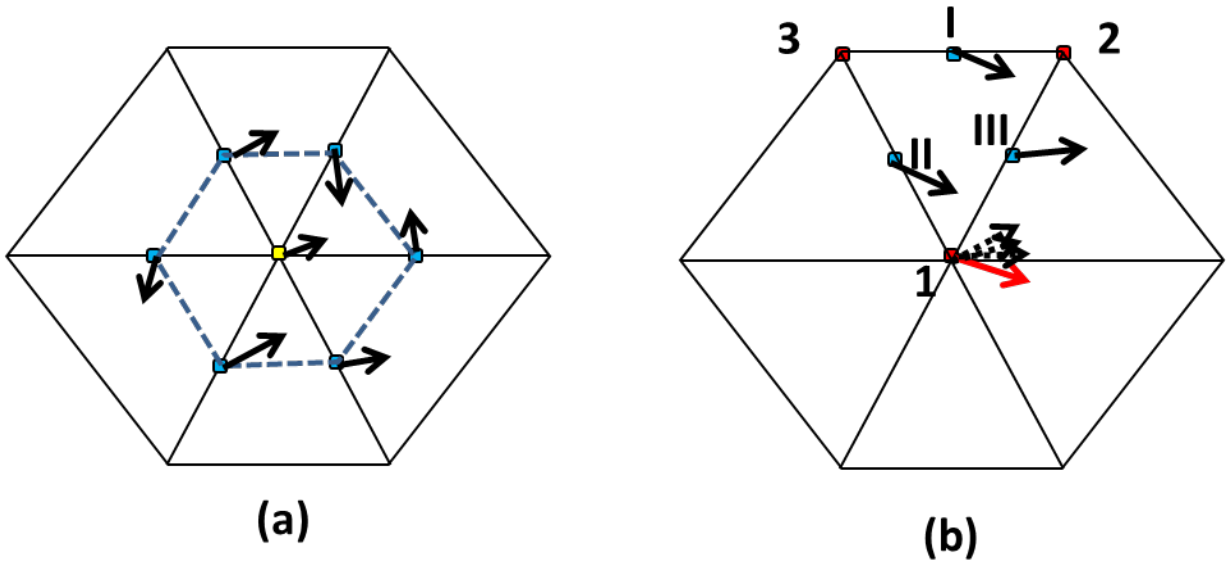

Fig. 4: Two methods of converting side velocities to a node velocity. (a) Inverse distance interpolation from sides (blue dots) to node (yellow dot); (b) use of FEM shape function to find the node velocity within each element first (the red arrow), i.e. $\mathbf{u}_1=\mathbf{u}_{II}+\mathbf{u}_{III}-\mathbf{u}_I$, followed by a simple averaging method to calculate the final value from all of its surrounding elements (dashed arrows).

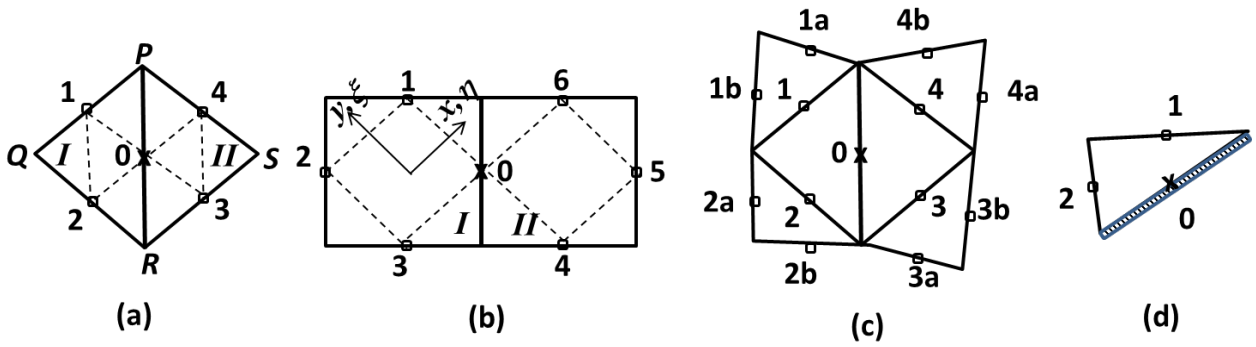

Fig. 5: Shapiro filters for (a) triangular and (b) quadrangular elements. The same stencils are used to construct the viscosity. '*I*' and '*II*' are 2 adjacent elements of side of interest ('0'). The extended stencil used in constructing bi-harmonic viscosity is shown in (c). The special case of a boundary side is shown in (d).

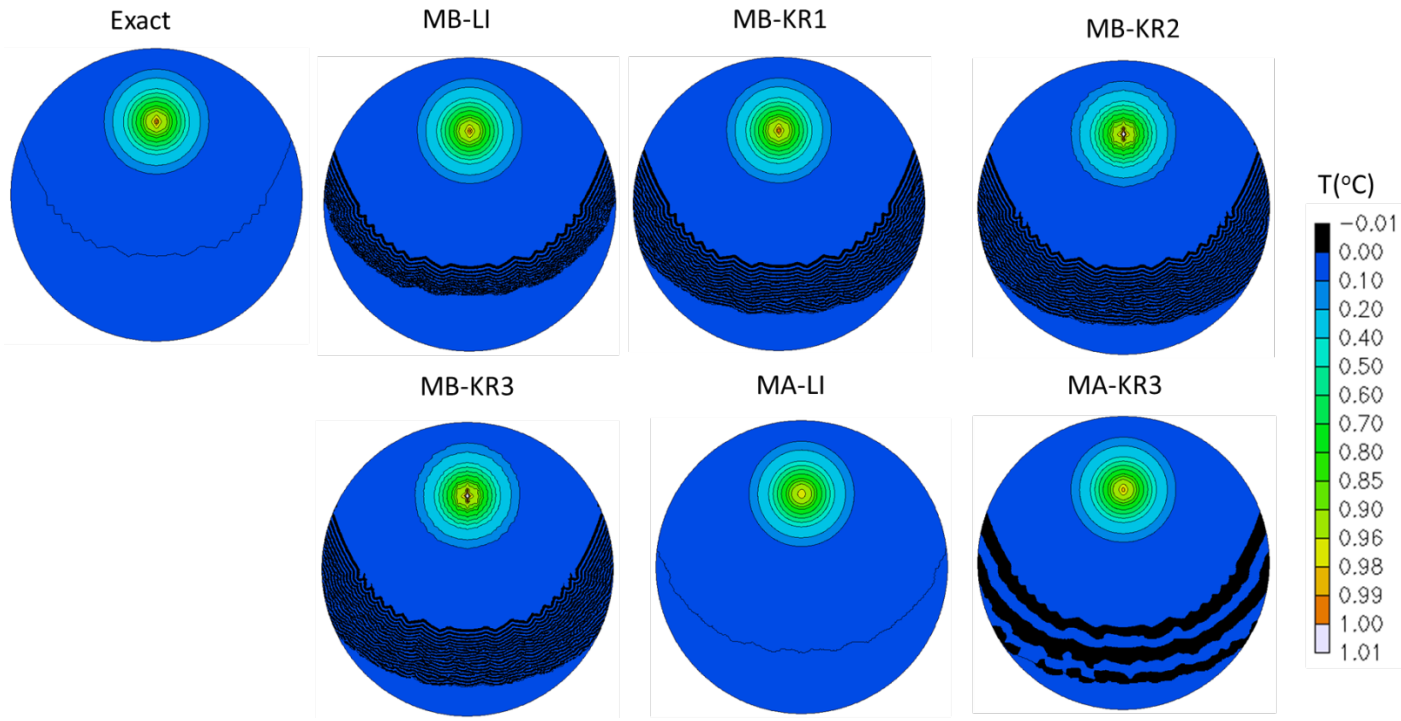

Fig. 6: Temperature after 1 rotation in the rotating Gauss hill test from various schemes with Δx=50m. ELAD filter is applied to all 'KR' schemes.

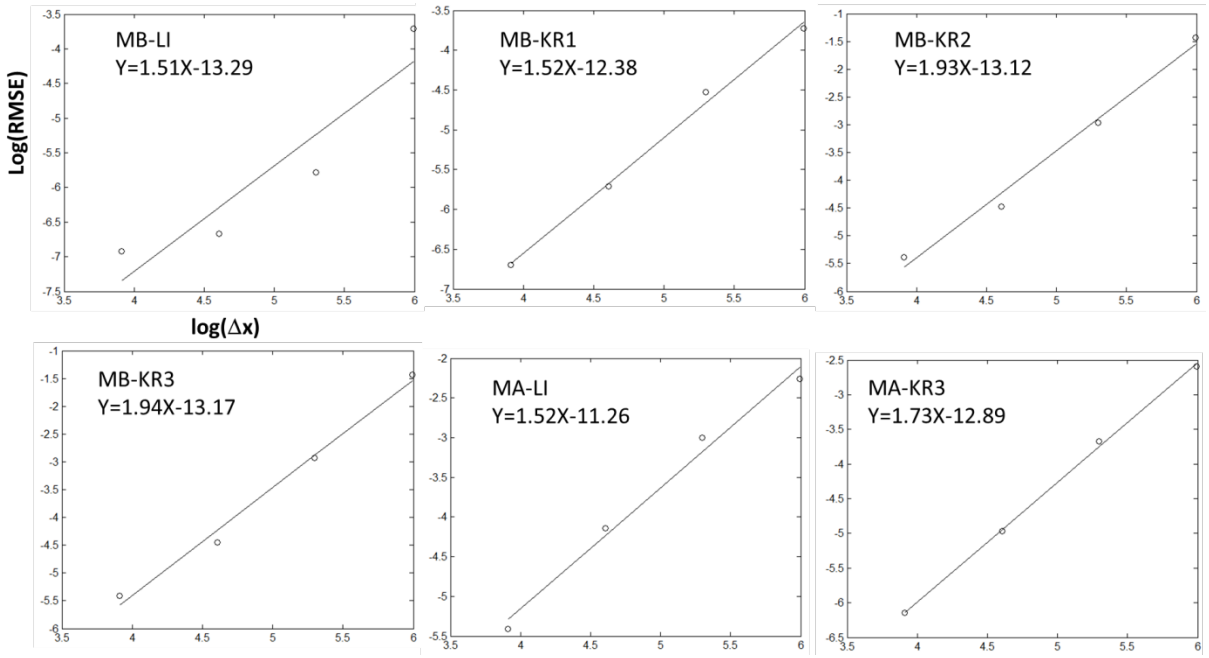

Fig. 7: Convergence curves of various advection schemes. The equations in each panel are linear regression fit. The intersection with *x*-axis in each equation is related to the coefficient of leading-order truncation error, and MB-LI has the smallest value.

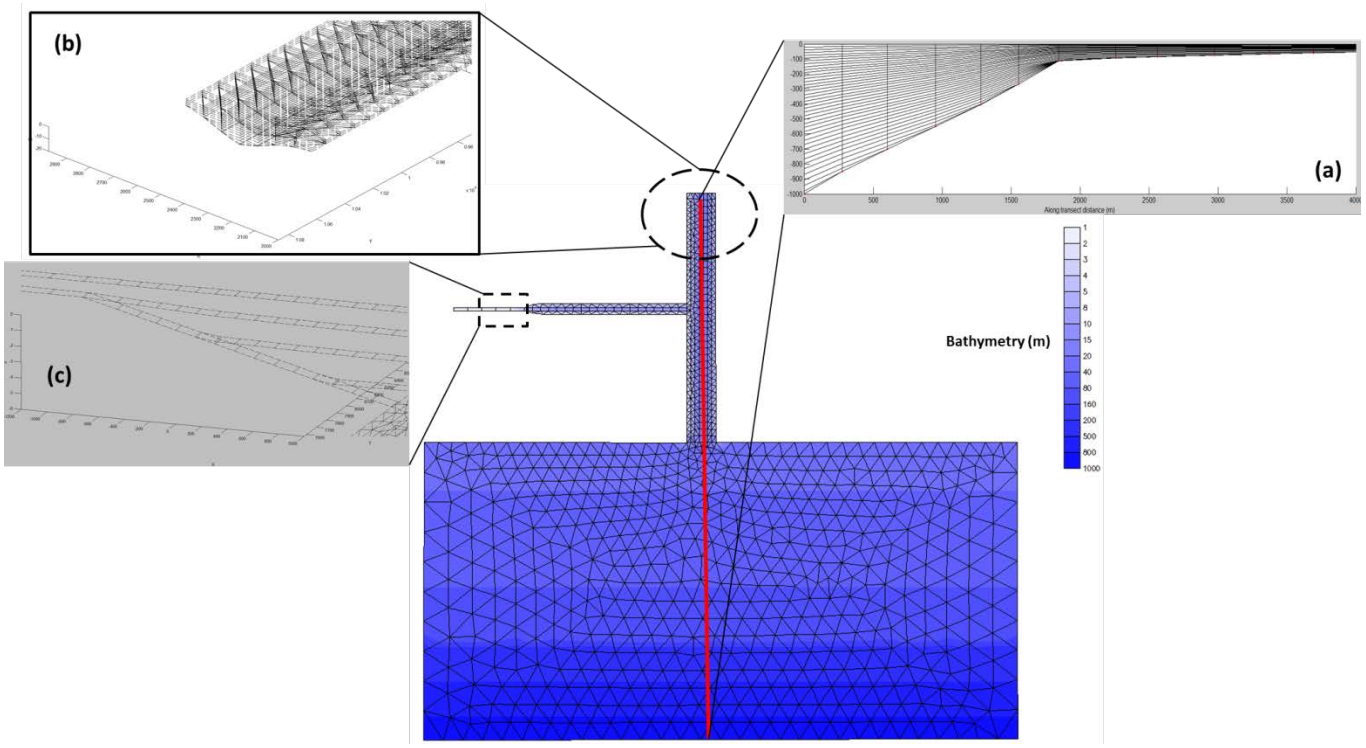

Fig. 8: Model polymorphism illustrated with a toy problem. The mixed triangular-quadrangular grid and the bathymetry are shown in the foreground. The vertical transect grid along the redline going from deep ocean into estuary ('shipping channel') is shown in insert (a). The 3D view of the grid near the head of estuary is shown in insert (b), with few layers on the shallow shoals. The grid near the upstream river is shown in insert (c), where transition from 2DV to 1D grid can be seen. In the test, a M2 tide is applied at the ocean boundary, and fresh water discharges are imposed at the heads of the river and estuary.

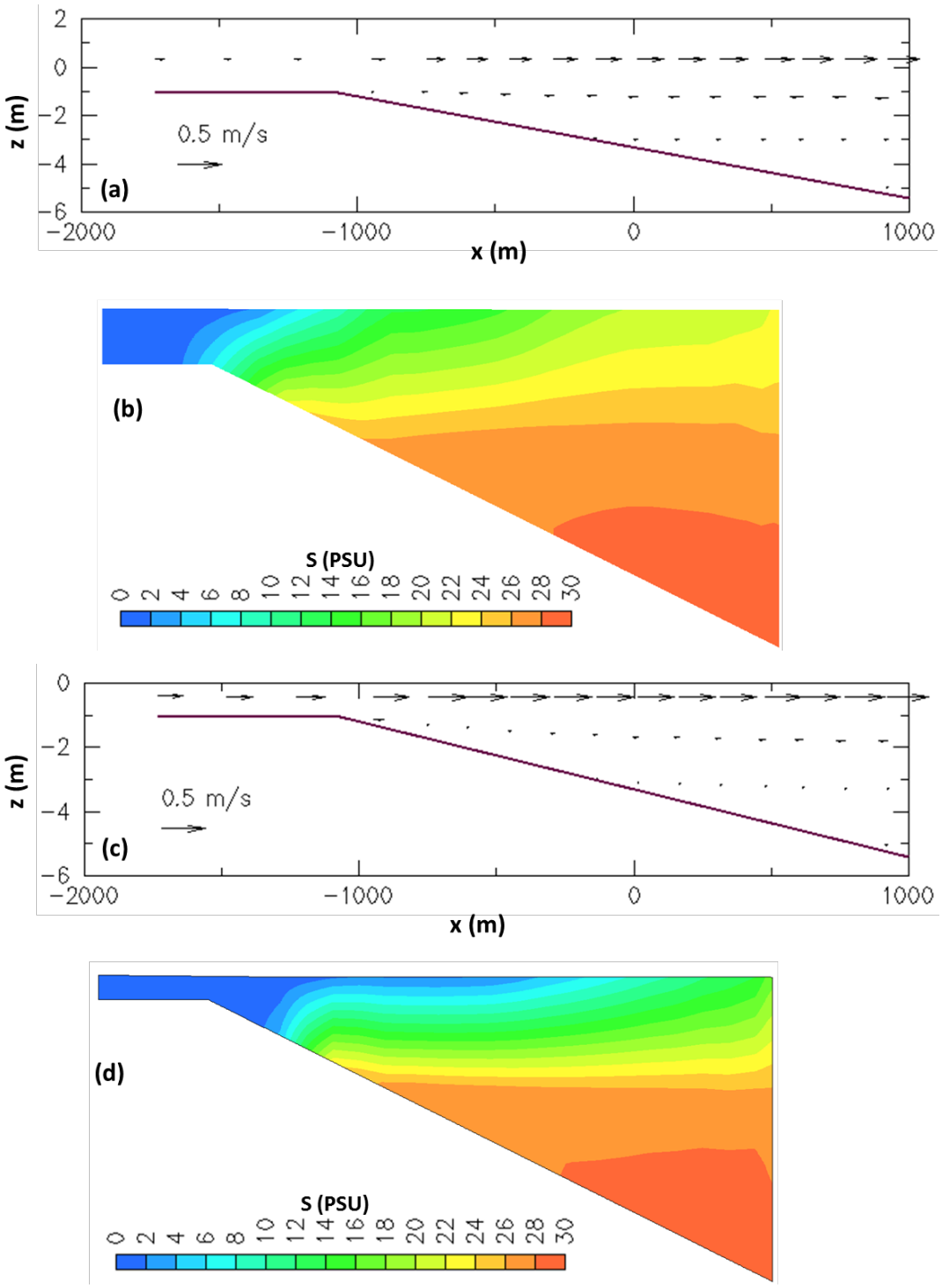

Fig. 9: Snapshot of velocity (a&c) and salinity (b&d) along the river transect (cf. Fig. 8c) showing the transition from 2DV to 1D region (i.e. the flat portion on the left). (a&b) correspond to a peak flood and (c&d) a peak ebb. The uni-directional river flow can be seen even during flood, and the tilt of isohaline line in (b) into the 1D zone is due to the linear interpolation of colors used in plotting; otherwise the 1D zone shows a uniform salinity/velocity along the vertical column. The burgundy line in (a&c) is the bottom.

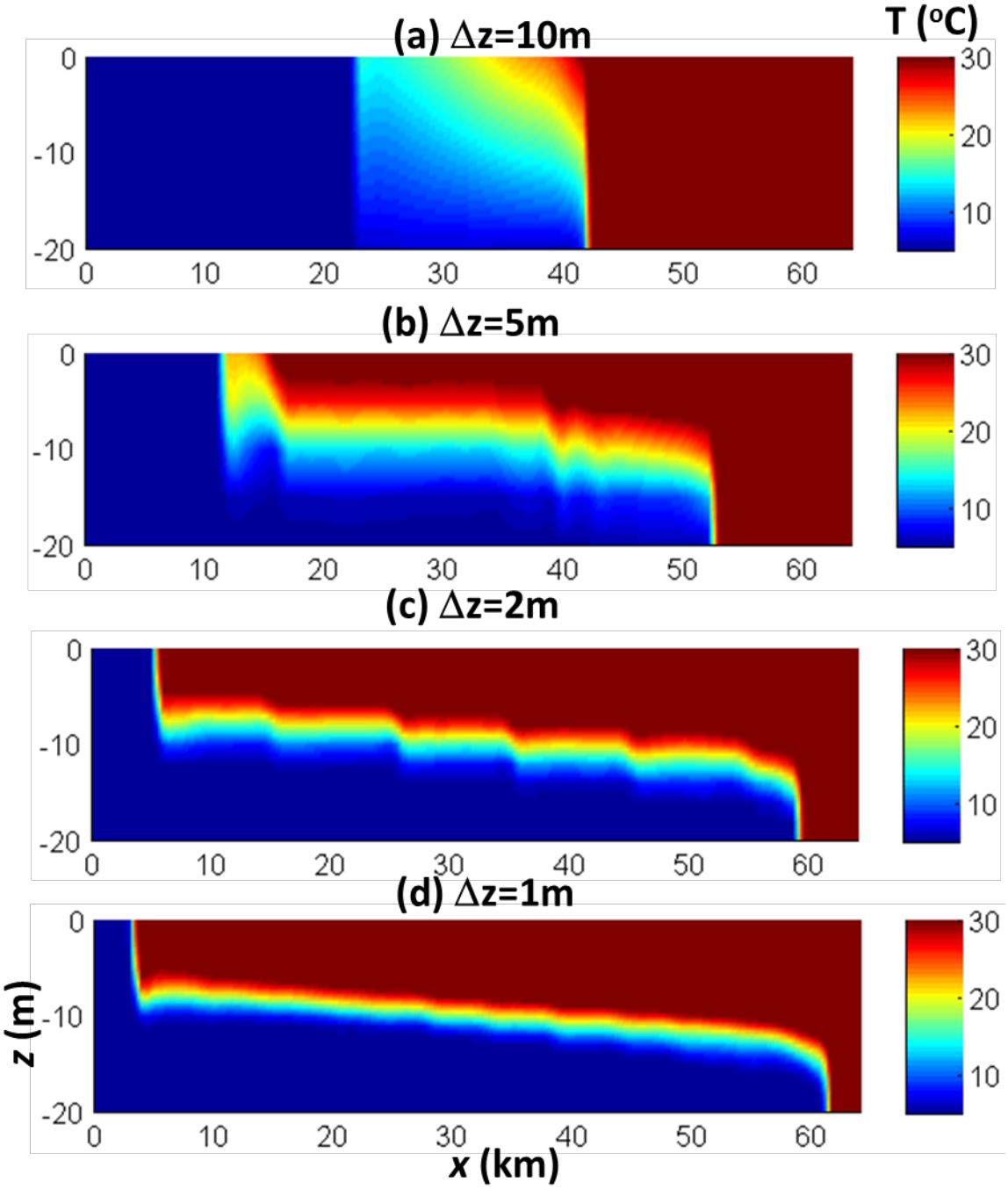

Fig. 10: Vertical transects of temperature at *t*=17 hours, with vertical resolution of 10, 5, 2 and 1m. The horizontal resolution is fixed at 500m.

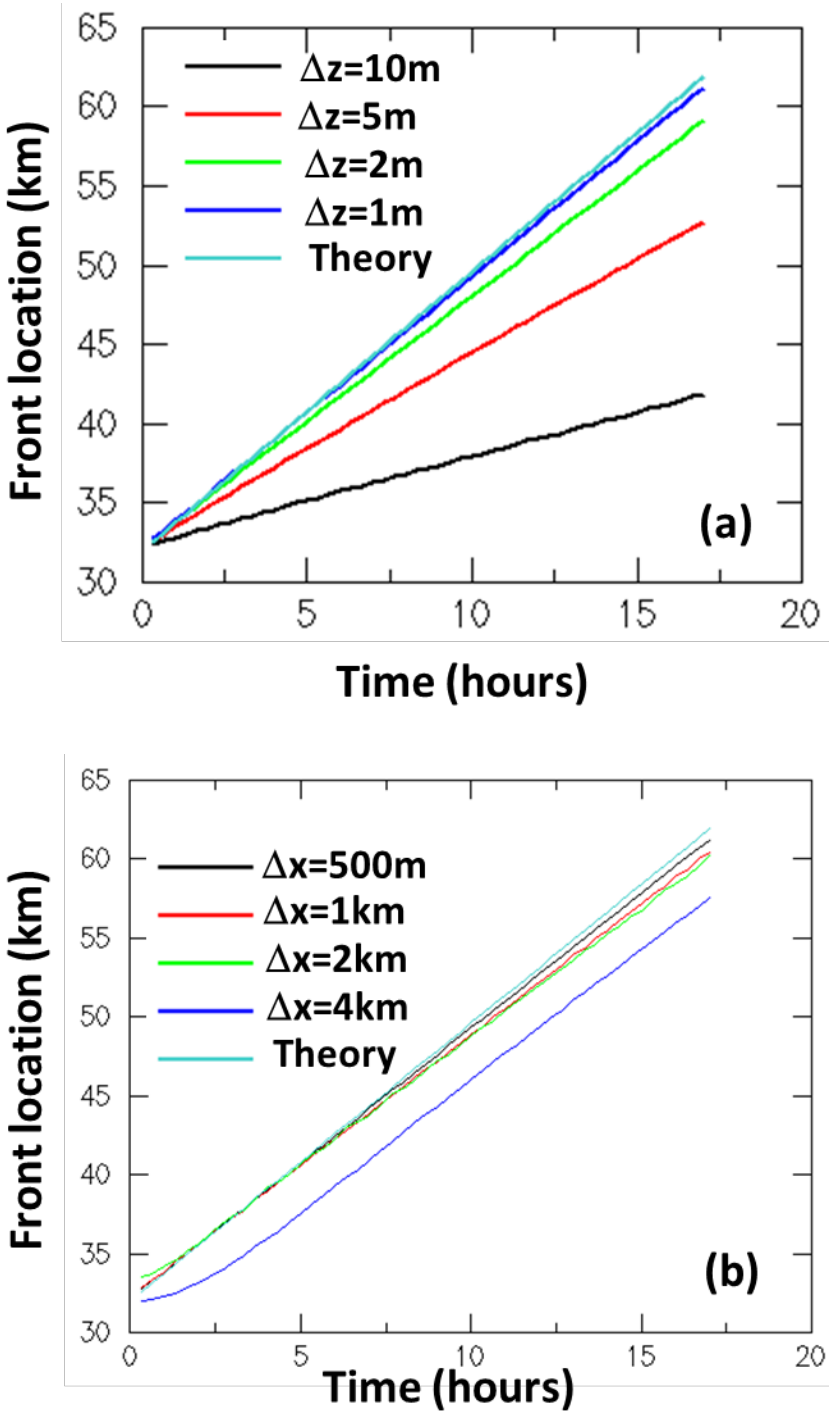

Fig. 11: Time history of front location from (a) different vertical resolution (with horizontal resolution fixed at 500m); (b) different horizontal resolution (with vertical resolution fixed at 1m). The theoretical results of Benjamin (1968) are also shown.

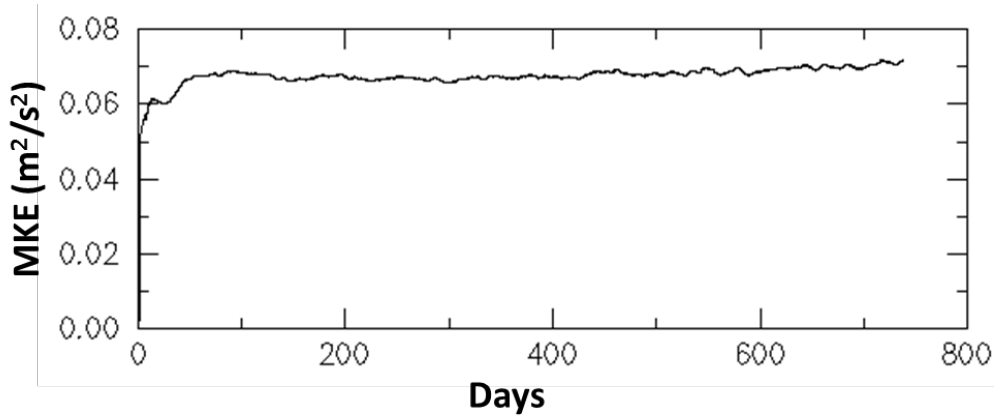

Fig. 12: Simulated mean kinetic energy (doubled kinetic energy scaled by mass) over time.

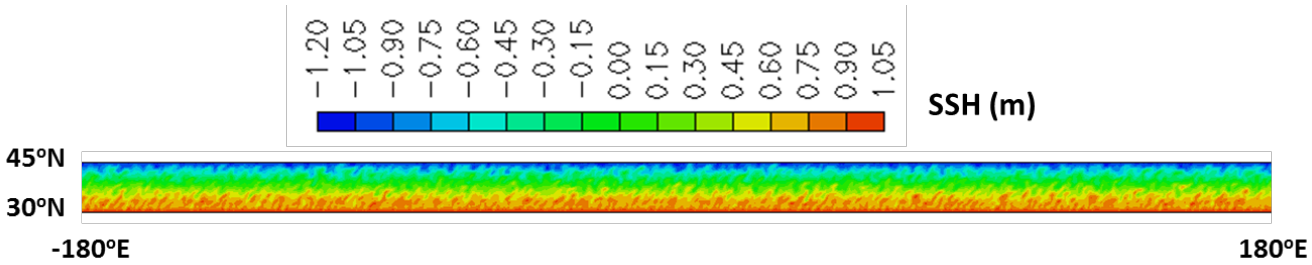

Fig. 13: Snapshot of SSH for the entire grid showing periodicity along the zonal band.

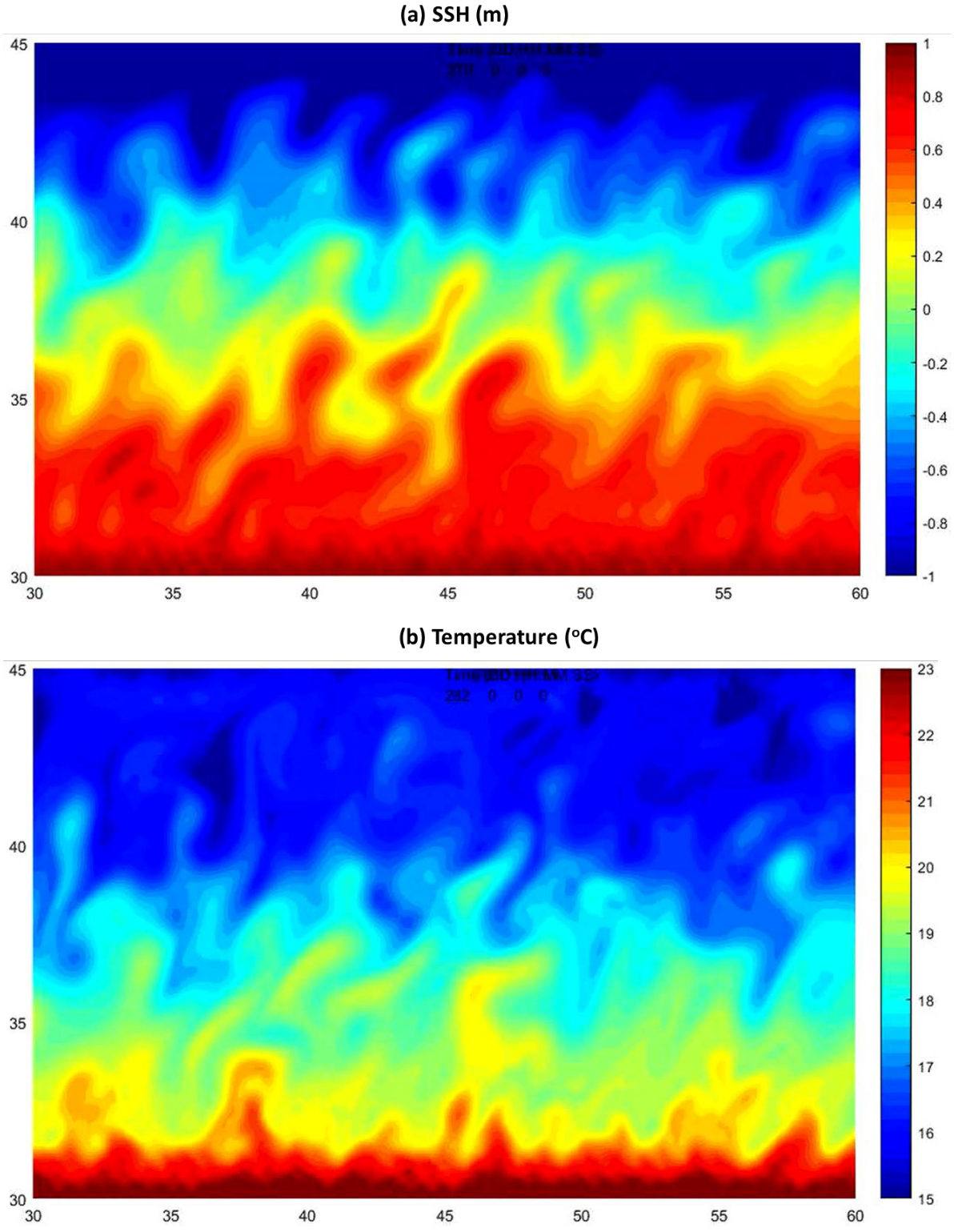

Fig. 14: Snapshot of (a) SSH, (b) temperature at 100m depth, and (c) relative vorticity (scaled by local Coriolis
706 parameter) at 100m depth

Fig. 15: (a) Black Sea bathymetry. Also shown are major geographic names and rivers around Black Sea (Sakarya, 708 Kizilirmak, Rioni, Dniepr, Dniestr, and Danube) and Azov Sea (Don and Kubon). (b) Bottom slope $((\partial\partial h/\partial\partial\partial)_2+(\partial\partial h/\partial\partial\partial)_2)$ of Black Sea, with values larger than 0.05 (1:20) being highlighted. (c) Hannah-Wright ratios, with values larger than 0.1 being highlighted. (d) SCHISM grid for Black Sea showing the placement of nodes. Uniform resolution of 3km is used except near the exit to Bosphorus Strait.

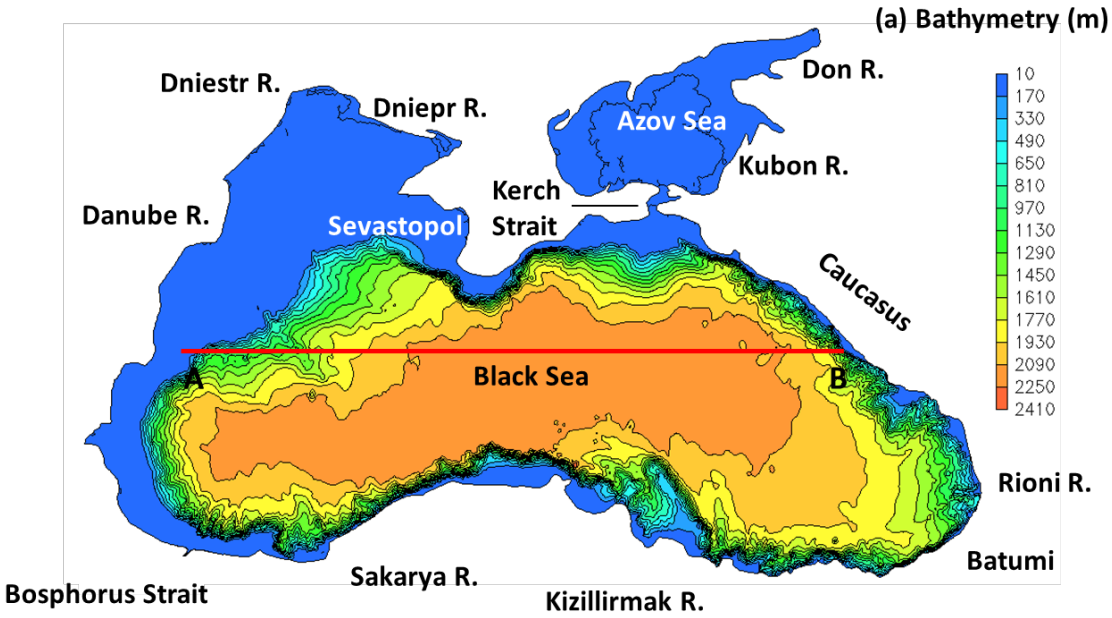

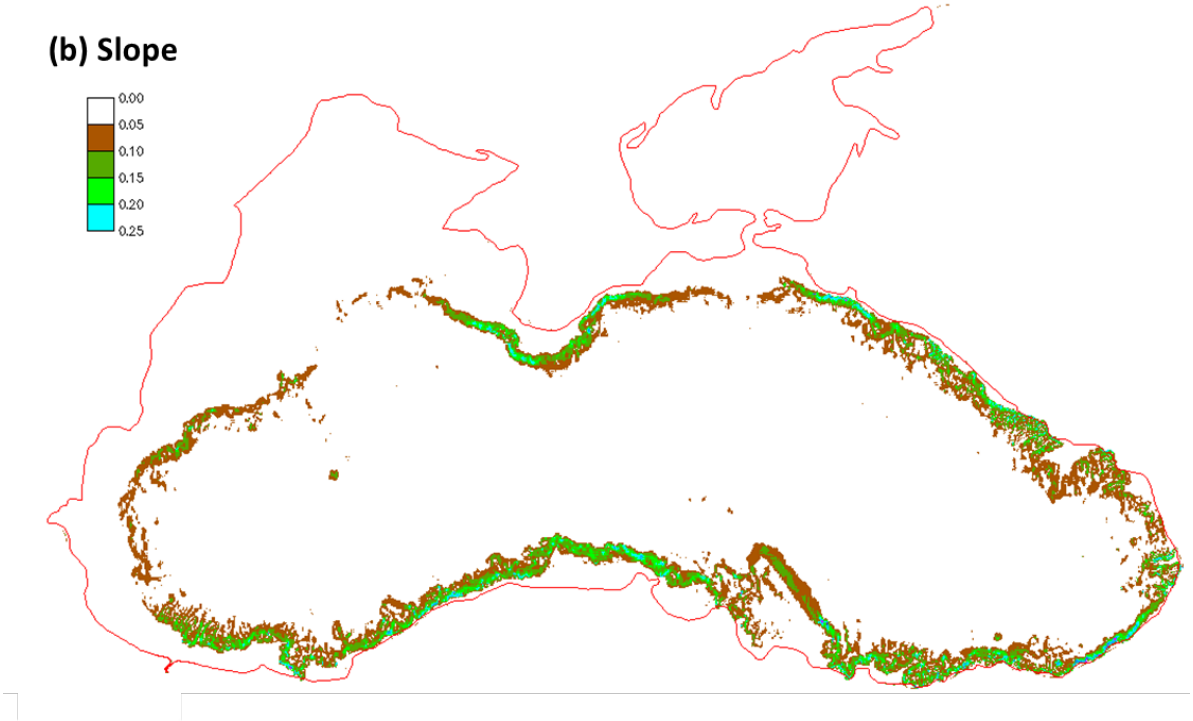

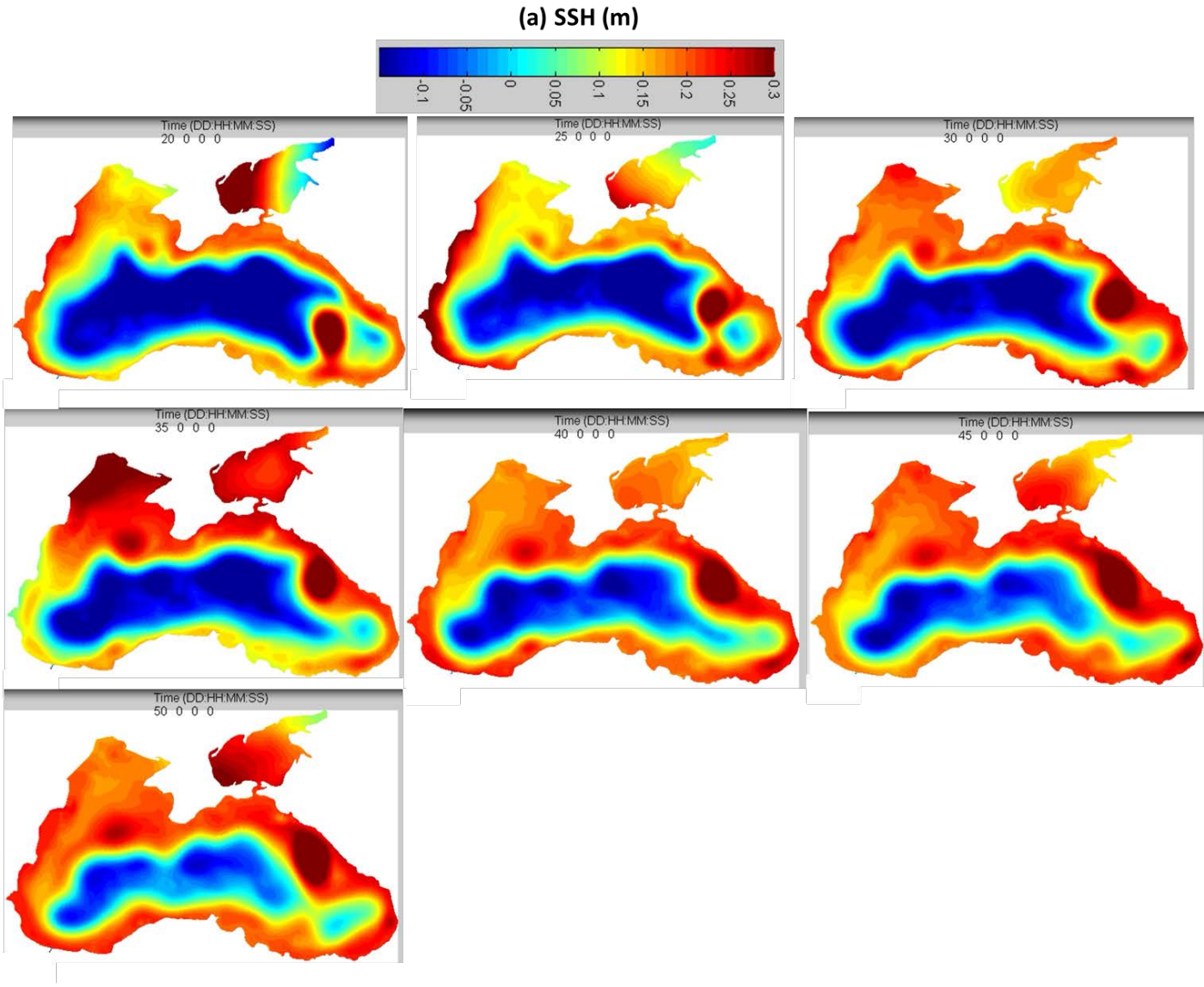

Fig. 16: Snapshots of SSH from (a) SCHISM; (b) SELFE. The time stamps are shown near the top of each panel. Major eddies in Black Sea can be seen in (a) and compared with Stanev (2005).